International Journal of Heat and Mass Transfer 115 (2017) 1258–1275

Contents lists available at ScienceDirect

International Journal of Heat and Mass Transfer

journal homepage: www.elsevier.com/locate/ijhmt

Pressure drop characteristics of large length-to-diameter two-phase micro-channel heat sinks

Seunghyun Lee, V.S. Devahdhanush, Issam Mudawar *

Purdue University Boiling and Two-Phase Flow Laboratory (PU-BTPFL), Mechanical Engineering Building, 585 Purdue Mall, West Lafayette, IN 47907, USA

ARTICLE INFO

Article history:
Received 16 May 2017
Received in revised form 27 August 2017
Accepted 28 August 2017
Available online 8 September 2017

Keywords:
Micro-channel
Heat sink
Flow boiling
Pressure drop
Flow patterns
Flow oscillations

ABSTRACT

Unlike prior published two-phase micro-channel studies that concern mostly miniature heat sinks, the present study addresses transport characteristics of a heat sink containing large length-to-diameter micro-channels. The copper heat sink has a 609.6-mm long by 203.2-mm wide base area, and contains 100 parallel micro-channels having a 1×1 mm^2 cross-section, and a length-to-diameter ratio of 609.6 to 1. The study addresses pressure drop characteristics of R134a for subcooled inlet conditions with inlet pressures of 689.4–731.3 kPa, mass velocities of 75.92–208.79 kg/m^2 s, and base heat fluxes of 4036–28,255 W/m^2. The data are compared to predictions of the Homogeneous Equilibrium Model (HEM) in conjunction with six different two-phase mixture viscosity relations, correlations based on the Separated Flow Model (SFM) and intended for macro-channels, and correlations based on SFM and intended for micro-channels. Overall, fairly good predictions are achieved with HEM, compared to poor predictions with the macro-channel SFM correlations. The micro-channel SFM correlations fared better, yielding mean absolute error values as low as 6.66%. Flow visualization results show appreciable periodic fluctuations in two-phase flow patterns, which include four primary patterns: *bubbly/slug*, *slug*, *transition*, and *annular*, along with two other patterns associated specifically with downstream dryout: *transition* and *annular*. These observations point to the need for more research to address the role of flow instabilities and fluctuations in flow pattern development.

1. Introduction

1.1. High-flux thermal management schemes

Development of many modern thermal devices is facing a myriad of challenges, including compact and lightweight design, and, most importantly, ability to dissipate enormous amounts of heat from small surface areas while maintaining relatively low surface temperatures. In the past, these challenges were adequately met with a variety of finned air-cooled surface attachments, and in more demanding situations, single-phase liquid cooling schemes. But further escalation in heat dissipation prompted a shift to two-phase cooling schemes, which, unlike single-phase schemes that rely on sensible heat rise to dissipate the heat, capitalize on both sensible and latent heat of the working fluid. Aside from their ability to dissipate much higher heat fluxes, two-phase schemes produce comparatively mild changes in surface temperature corresponding to large fluctuations in the heat flux [1].

A variety of two-phase cooling schemes have been proposed, whose design is based not only on thermal requirements but packaging concerns as well. Initially, efforts were focused on incorporating capillary-driven two-phase devices. But these devices pose many challenges, including relatively low to moderate heat flux, limited thermal span for conventional heat pipes [2,3], and startup issues for capillary pumped loops and loop heat pipes [4]. A popular passive cooling alternative to capillary-driven devices is thermosyphons, which rely on simultaneous pool boiling and condensation as well as buoyancy to achieve the required thermal performance. Thermosyphons provide a variety of advantages, including low cost, passive coolant circulations, and adaptability to cooling both small and large heat-dissipating packages. Additionally, their performance can be greatly enhanced by modifying the surface with micro-grooves, micro-fins, or extended surfaces [5–7]. Nonetheless, these strategies are often insufficient at handling the high heat fluxes encountered in many modern applications.

With these shortcomings, two-phase thermal management has recently shifted to active cooling schemes, which utilize a mechanical pump to circulate the coolant. The generic advantage of these schemes is their ability to enhance cooling performance by faster

* Corresponding author.
E-mail address: mudawar@ecn.purdue.edu (I. Mudawar).
URL: https://engineering.purdue.edu/BTPFL (I. Mudawar).

http://dx.doi.org/10.1016/j.ijheatmasstransfer.2017.08.104

Nomenclature

A	cross-sectional area of flow channel
A_{base}	total base area of heat sink
B	coefficient in Chisholm correlation
Bd	Bond number
Bo	boiling number
C	parameter in Lockhart-Martinelli correlation
C_c	contraction coefficient
c_p	specific heat at constant pressure
D	diameter
D_h	hydraulic diameter
f	friction factor
f_{app}	apparent friction factor
Fr	Froude number
G	mass velocity
g	gravitational acceleration
h	enthalpy
H_{ch}	micro-channel height
h_{fg}	latent heat of vaporization
H_p	plenum height
j	superficial velocity
k	exponent in Chisholm correlation
L	length; micro-channel length
MAE	mean absolute error (%)
$\dot{m}$	mass flow rate through micro-channel
N_{ch}	number of micro-channels in heat sink
N_{conf}	Confinement number
p	pressure
P_F	frictional perimeter
P_H	heated perimeter
Δp	pressure drop
Q	heat input
q''_B	heat flux based on total base area of heat sink
q''_H	heat flux based on heated perimeter of micro-channel
Re	Reynolds number
Su	Suratman number
T	temperature
u	velocity
v	specific volume
$\bar{v}$	specific volume of two-phase mixture
v_{fg}	specific volume difference between vapor and liquid
W_{ch}	micro-channel width
We	Weber number
W_p	plenum width
X	Lockhart-Martinelli parameter
x	vapor quality
x_e	thermodynamic equilibrium quality
z	coordinate along flow direction

Greek symbols

α	void fraction
β	aspect ratio of micro-channel, $\beta = W_{ch}/H_{ch}$
Γ	parameter in Chisholm correlation
δ	thickness of hydrodynamic boundary layer
δ^+	dimensionless thickness of hydrodynamic boundary layer
θ	percentage predicted within ±30%
λ	paramer in Lee and Lee correlation
μ	viscosity
ξ	percentage predicted within ±50%
ρ	density
$\bar{\rho}$	density of two-phase mixture
ρ_H	two-phase mixture density based on Homogeneous Equilibrium Model
σ	surface tension; standard deviation
σ_c	contraction area ratio
σ_e	expansion area ratio
τ	wall shear stress
ϕ^2	pressure drop multiplier
ψ	paramer in Lee and Lee correlation
ω	coefficient in Beattie and Whalley viscosity model

Subscripts

A	accelerational
avg	average
c	inlet contraction
e	exit expansion
exp	experimental (measured)
F	frictional
f	liquid
fo	liquid only
G	gravitational
g	vapor
go	vapor only
in	micro-channel inlet
k	liquid (f) or vapor (g)
out	micro-channel outlet
$pred$	predicted
sat	saturation
sp	single phase
tp	two phase
tt	turbulent liquid-turbulent vapor
tv	turbulent liquid-laminar vapor
vt	laminar liquid-turbulent vapor
vv	laminar liquid-laminar vapor

fluid motion. The most basic of these schemes are macro-channel flow boiling [8–12] and those utilizing falling films [13]. However, there is now consensus that the most effective two-phase cooling schemes are those utilizing micro-channel flow, jet impingement, and sprays [14]. Even more effective are ‘hybrid cooling schemes’ combining the merits of micro-channel flow boiling and jet impingement [15].

Jet-impingement has been used in a broad variety of applications demanding highly concentrated heat removal, but is known to produce large gradients in the heat-dissipating surface [16]. And while they require only moderate pressure drop (mostly across the jet nozzle) [17], they demand large coolant flow rates, especially when implemented in multi-nozzle arrangements; such arrangements are also known to induce unpredictable flow and instabilities in the spent fluid emanating between adjacent impingement zones.

Spray cooling is often deemed a competitor to jet-impingement cooling. Its primary advantage compared to the latter is better surface temperature uniformity, brought about by breaking the liquid flow into fine droplets prior to the surface impact. These droplets acquire a broad range of trajectories, ensuring better surface temperature uniformity than with jet impingement [18–22]. Overall, spray cooling requires higher pressure drop but lower coolant flow rate than jet impingement. An important drawback of spray cooling is dependence of its cooling performance on an unusually large number of parameters (nozzle design, cone angle, nozzle-to-surface distance, inlet subcooling, flow rate, *etc.*), rendering spray performance far more difficult to predict compared to micro-channel cooling or jet-impingement.

1.2. Two-phase micro-channel cooling

Aside from their ability to tackle very high heat transfer coefficients (mostly because of small hydraulic diameter) and high critical heat flux (CHF), two-phase micro-channel cooling also greatly decreases size and weight of cooling hardware, and minimizes coolant inventory requirements [23–27]. They also provide great adaptability to very high heat flux situations, such as water cooling of industrial turbine blades and fusion reactors, with heat fluxes in excess of 10^3 and 10^4 W/cm^2, respectively. Most notably, Bowers and Mudawar experimentally achieved CHF values up to 27,600 W/cm^2 using highly subcooled and high mass velocity water flow through small diameter tubes [28,29]. Another interesting development is the ability to incorporate micro-channel heat sinks into pumpless two-phase loops [30]. However, as indicated by Bowers and Mudawar, design of micro-channel heat sinks requires a very thorough understanding of pressure drop and heat transfer characteristics in order to avoid such complications as (1) high compressibility, (2) flashing, (3) two-phase choking, (4) flow instabilities, and (5) pre-mature CHF [23].

To alleviate the shortcomings of micro-channel flow boiling, efforts in recent years have been focused on (1) amassing new databases for different working fluids and channel geometries, aided by high speed video capture of interfacial behavior, and (2) developing improved methods for prediction of pressure drop, heat transfer coefficient, and CHF. Most of these studies involve micro-channel heat sinks containing many parallel micro-channels that are formed into a thermally conducting substrate. Pressure drop in these studies is assessed using a variety of predictive methods, including several variations of the Homogeneous Equilibrium Model (HEM) and Separated Flow Model (SFM), as well as empirical formulations. A few theoretical models have also been proposed for heat sinks incurring annular flow [23].

1.3. Objectives of present study

While most prior studies addressing the transport characteristics of two-phase micro-channels have focused on small heat sinks compatible with electronics devices, the present study is focused on much larger heat sinks containing parallel large length-to-diameter micro-channels. The present study concern pressure drop characteristics of these heat sinks.

This study is motivated by the need to develop multi-kilowatt evaporators for future space vehicles that could tackle heat removal from both avionics and crew. As discussed in [31–33], adaptation of flow boiling in reduced gravity situations poses a host of unique fundamental and practical challenges. A recent study by the authors [34] addressed the challenges of incorporating large area micro-channel heat exchangers as evaporators in Hybrid Thermal Control Systems (H-TCS) to tackle the heat removal in space vehicle. The H-TCS allows the two-phase hardware to be automatically reconfigured into a vapor compression loop, a pumped two-phase cooling loop, or a pumped single-phase loop. In follow-up studies, the authors examined local heat transfer characteristics of a large area micro-channel heat sink using a vapor compression TCS [35,36], as well as related practical implementation concerns [37].

This present study concerns implementation of a large area micro-channel heat sink utilizing the pumped loop configuration of the H-TCS. A unique aspect of this study compared to the majority of prior investigations of two-phase micro-channel heat sinks is large length-to-diameter ratio. The long micro-channels investigated here provide a broad axial span along which detailed evolution of interfacial features and flow patterns may be carefully measured and captured via high-speed video. Large micro-channel length also represents a very valuable parameter that can aid in the assessment of prior correlations developed for relatively short micro-channels. The main objectives of this study are as follows:

1. Perform detailed experimental investigation of the influence of key flow parameters on micro-channel pressure drop.
2. Assess the accuracy of several variations of HEM and SEM, the latter including formulations for macro-channels and micro-channels, against the experimental data.
3. Explore transient variations of local flow regimes and pressure drop for different operating conditions.

2. Experimental methods

2.1. Two-phase flow loop

Fig. 1 shows a schematic diagram of the two-phase cooling loop that is configured to condition the working fluid, R134a, to desired operating conditions at the inlet to the micro-channel module. This fluid is selected based on a number of considerations, including the loop's thermodynamic performance, maximum system pressure, flow rate requirements, and both safety and environmental concerns [34]. Shown in Fig. 2(a) and (b) are, respectively, front view and rear view 3D-CAD renderings of the entire test facility.

Both heat transfer measurement and high-speed video analysis are performed with the micro-channel module. Within this module, heat is supplied to the fluid from a thick film heater situated beneath a micro-channel heat sink. The electrical power input is supplied by an auto-transformer and measured by a power meter. The power input causes the liquid entering the micro-channel module to undergo gradual change of phase along the micro-channels. As shown in Fig. 1, the two-phase mixture exiting the micro-channel module is routed into a Trenton air-cooled condenser, where the fluid is brought to subcooled liquid state by rejecting heat to ambient air. Heat rejection from the condenser and the temperature of fluid exiting the condenser are adjusted by controlling the condenser's fan speed using a solid-state controller connected to a permanent split capacitor motor. Pressure within the flow loop is adjusted mainly by a PID controller that receives signals from a pressure transducer mounted at the condenser outlet, and power input to an electric heater submerged in the loop's liquid reservoir. The reservoir's pressure serves as a set point for the flow loop. A Lytron modular cooler supplies cold water through a helical coiled tube inside the vessel, which condenses the R134a vapor to liquid state. Liquid R134a is subcooled further through a SWEP plate-type heat exchanger that is connected to a second Lytron modular cooler, to make certain that no vapor is routed to the downstream pump or turbine flow meter. The fluid is circulated within the loop using a GB series magnetic drive gear Micropump, which is driven by a Baldor 3-phase motor and controlled by a VS1MX AC duty Microdrive. Volumetric flow rate is measured by the turbine flow meter before passing through a manual control valve followed by the micro-channel module.

2.2. Construction of Micro-channel module

Fig. 3(a) shows a 3D CAD diagram illustrating the detailed layered construction of the micro-channel module. The main component of the module is an oxygen-free copper heat sink having a 609.6-mm long by 203.2-mm wide top surface. Machined into the top surface are 100 parallel micro-channels having a 1×1 mm^2 cross-section. Uniform heat flux is supplied to the heat

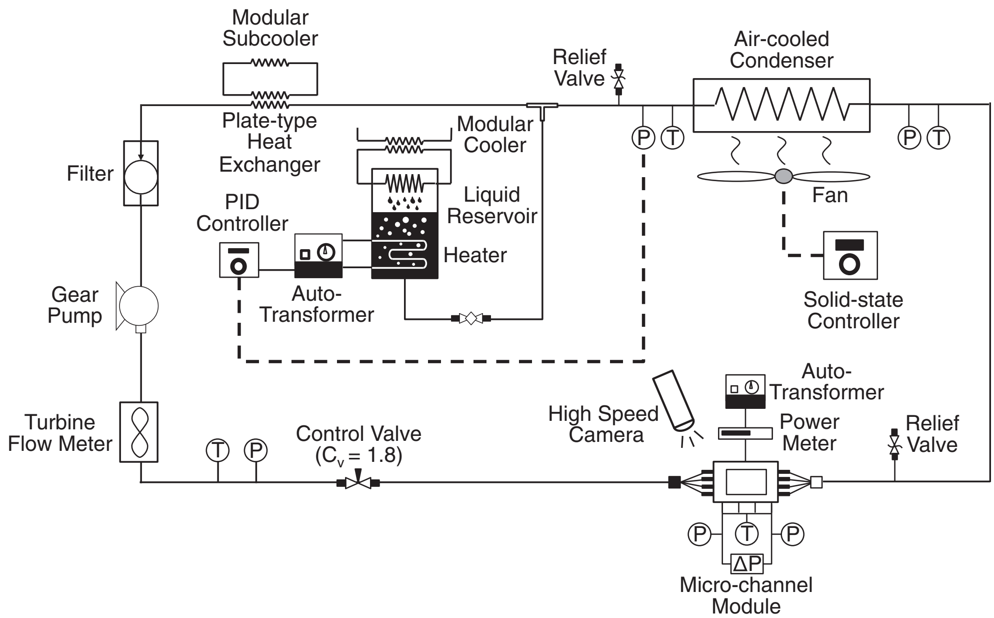

Fig. 1. Schematic diagram of two-phase loop.

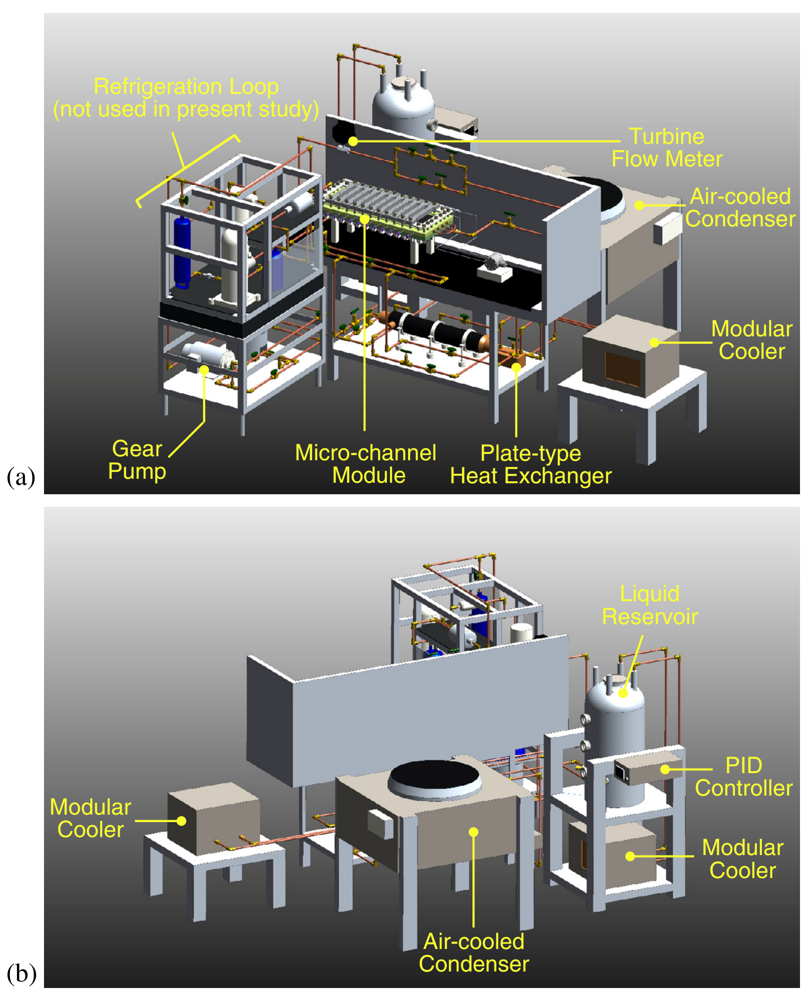

Fig. 2. 3D CAD drawings of test facility: (a) front view (b) rear view.

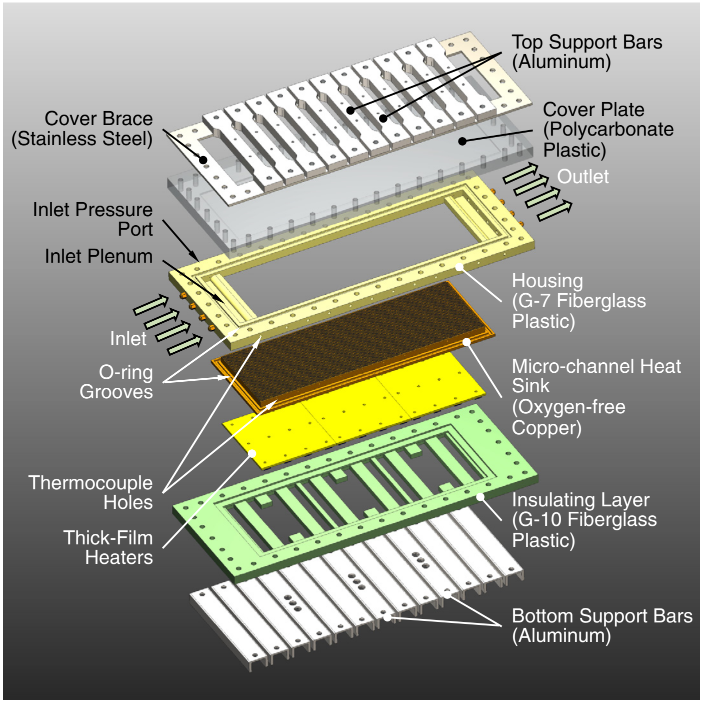

(a)

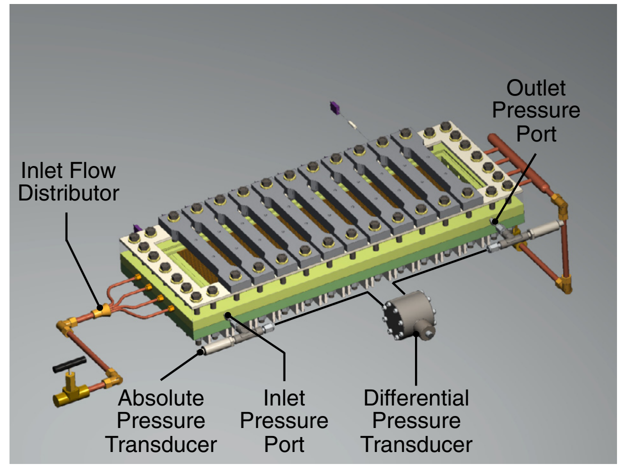

(b)

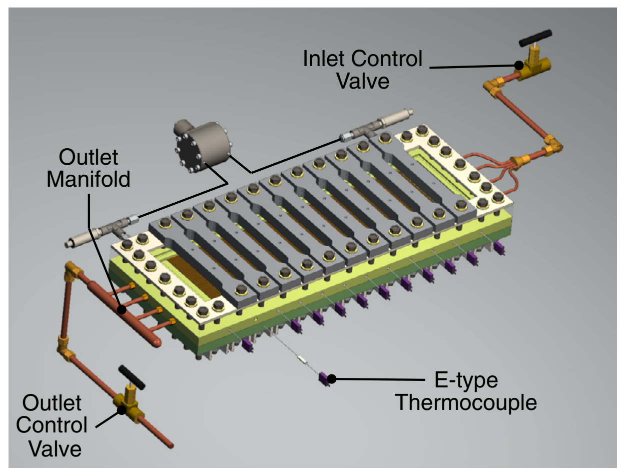

(c)

Fig. 3. (a) Construction of micro-channel module. (b) Frontal view showing inlet flow manifold and pressure instrumentation. (c) Rear view showing temperature instrumentation and outlet manifold.

sink using a Watlow thick-film heater. The copper heat sink temperatures are measured with type-E thermocouples at several axial locations provided in Table 1. The heat sink and thick film heater are contained in an insulating housing made from G-7 fiberglass and insulated beneath by a layer of G-10 fiberglass. The tops of the micro-channels are closed off by a transparent cover plate made from polycarbonate plastic (Lexan), which provides optical access to the two-phase flow along the micro-channels. The multiple layers of the micro-channel module are pressed tightly together using a stainless steel cover brace and aluminum support bars atop, as well as aluminum support bars below.

As shown in Fig. 3(b) and (c), the inlet and outlet plenums of the micro-channel module possess four flow ports each, which serve to enhance uniformity of flow distribution among the micro-channels. Each of the flow ports contains a Sporlan Venturi throat flow distributor and a custom flow manifold.

Table 1
Dimensions of the copper micro-channel heat sink and axial locations of the heat sink thermocouples.

Length [mm]	Width [mm]	Number of channels	Thermocouple axial locations [mm]
609.6	203.2	100	44.2, 102.1, 160.0, 217.9, 275.8, 333.8, 391.7, 434.3, 507.5, 565.4

2.3. Measurement instrumentation and data acquisition

As shown in Fig. 3(b), pressure is measured at the inlet and outlet of the micro-channel module by a combination of two Omega-MMA absolute pressure transducers and a Honeywell-THE differential pressure transducer. As depicted in Fig. 3(c), temperature of the copper heat sink is measured at several axial locations with the aid of type-E thermocouples, which possess the highest Seebeck coefficient of 68 μV/°C among the different thermocouple types. Each thermocouple is inserted along a stainless steel sheath, with the junction set along the centerline of the copper heat sink.

Volumetric flow rate is measured by a Flow Technology FTO series turbine flow meter, which is installed in the single-phase liquid portion of the flow loop. A Yokogawa WT310 power meter is used to measure the voltage, current, and power input to the thick-film heater.

An FET multiplexer collects signals from the thermocouples, pressure transducers, flow meter, and power meter, which are processed by an HP 3852a data acquisition system. Measurement errors and uncertainty propagated in key calculated parameters (using root sum square method) are provided in Table 2.

Images of the two-phase flow along the micro-channel module are captured by a Photron-Ultima APX high-speed camera fitted with a 105-mm Nikkor lens. This camera is capable of shutter speeds as high as 1/120,000 s.

Table 2
Measurement error and uncertainty propagation.

Parameter	Error (%)	Parameter	Uncertainty (%)
Absolute pressure, p	±0.1	Heat transfer coefficient, h_{tp}	≤5.92
Differential pressure, Δp	±0.1	Pressure drop, Δp	≤0.1
Temperature, T	±0.5	Vapor quality change, Δx_e	≤3.23
Mass flow rate, $\dot{m}$	±0.12		
Heat input, Q	±0.3		

2.4. Operating conditions

The micro-channel module's inlet quality, $x_{e,in}$, is determined from the relation

$$x_{e,in} = \frac{h_{in} - h_f}{h_{fg}} = -\frac{c_{p,f}(T_{sat} - T_{in})}{h_{fg}}, \tag{1}$$

where $c_{p,f}$, T_{sat}, and h_{fg} are based on saturation pressure measured at the module's inlet, and T_{in} is the measured inlet temperature. The outlet quality is determined by applying an energy balance to the entire module,

$$x_{e,out} = x_{e,in} + (q''_B A_{base})/\dot{m} h_{fg}, \tag{2}$$

where q''_B is the heat flux based on the 609.6-mm long by 203.2-mm wide surface area, A_{base}, of the heat sink, and $\dot{m}$ the total flow rate of R134a. Table 3 provides the detailed operating conditions tested in this study.

3. Pressure drop predictive methods

3.1. Pressure drop components

The pressure drop measured by the pressure transducers in the micro-channel module's inlet and outlet plenums includes the sudden contraction loss and expansion recovery, respectively. Total pressure drop, Δp, across the module for subcooled inlet conditions also includes pressure drops associated with single-phase flow and two-phase flow across the micro-channels. The total pressure drop is expressed as

$$\Delta p = \Delta p_c + \Delta p_{sp,f} + (\Delta p_{tp,F} + \Delta p_{tp,G} + \Delta p_{tp,A}) + \Delta p_e, \tag{3}$$

where Δp_c, $\Delta p_{sp,f}$, $\Delta p_{tp,F}$, $\Delta p_{tp,G}$, $\Delta p_{tp,A}$, and Δp_e are pressure drop components associated, respectively, with inlet contraction pressure loss, upstream single-phase liquid flow, two-phase friction, two-phase gravity, two-phase acceleration, and outlet expansion recovery.The contraction loss and expansion recovery are expressed, respectively, as [38]

$$\Delta p_c = \frac{G^2 v_f}{2}\left[\left(\frac{1}{C_c} - 1\right)^2 + (1 - \sigma_c^2)\right]\left[1 + \frac{v_{fg} x_{e,in}}{v_f}\right], \tag{4}$$

where

$$\sigma_c = \frac{W_{ch} H_{ch} N_{ch}}{W_p H_p}, \tag{5}$$

and

$$\Delta p_e = G^2 \sigma_e (1 - \sigma_e) v_f \left[1 + \frac{v_{fg} x_{e,out}}{v_f}\right], \tag{6}$$

where

$$\sigma_e = \frac{W_{ch} H_{ch} N_{ch}}{W_p H_p}. \tag{7}$$

Notice that $W_{ch} = H_{ch} = 1$ mm in the present study. In Eq. (4), the contraction coefficient, C_c, associated with the Vena-contracta is a function of the area contraction ratio, σ_c, and obtained from a relation by Geiger [39],

$$C_c = 1 - \frac{1 - \sigma_c}{2.08(1 - \sigma_c) + 0.5371}. \tag{8}$$

The single-phase liquid pressure drop is expressed by

$$\Delta P_{sp,f} = \frac{2 f_{app} G^2 L_{sp,f} v_f}{D_h}, \tag{9}$$

where f_{app} is the apparent friction factor, which accounts for flow development effects in addition to liquid friction. For hydrodynamically developing laminar single-phase flow, f_{app} values are obtained from Shah and London [40], and fitted to a Churchill and Usagi [41] type empirical correlation. A continuous expression for f_{app} spanning both the developing and fully-developed single-phase regions was derived by Copeland [42],

$$f_{app} Re_{sp,f} = \left\{\left[3.2\left(\frac{L_{sp,f}}{Re_{sp,f} D_h}\right)^{-0.57}\right]^2 + (f_{sp,f} Re_{sp,f})^2\right\}^{1/2} \quad for \quad Re_{sp,f} < 2000, \tag{10}$$

where $f_{sp,f}$ is the friction factor for fully-developed single-phase flow through a rectangular channel with aspect ratio β (where $\beta < 1$), and is given by

$$f_{sp,f} Re_{sp,f} = 24(1 - 1.3553\beta + 1.9467\beta^2 - 1.7012\beta^3 + 0.9564\beta^4 - 0.2537\beta^5). \tag{11}$$

For hydrodynamically developing turbulent single-phase flow, the apparent friction factor is calculated using an analytical solution by Zhi-qing [43] for a circular tube based on $L_{sp,f}$, the axial extent of the turbulent single-phase region,

$$f_{app} = \left[\frac{1}{(1 - 0.25\delta^+ + 0.0667\delta^{+2})^2} - 1\right]\frac{0.25}{L_{sp,f}/D_h} \quad for \quad Re_{sp,f} \geqslant 2000, \tag{12}$$

Table 3
Operating conditions of micro-channel module.

G [kg/m^2 s]	q_B" [W/m^2]	$x_{e,in}$	$x_{e,out}$	p_{in} [kPa]	Number of Δp data points (69 total)
75.92	4005–10095	−0.031 to −0.022	0.331–0.893	688.3–690.0	4
94.90	3990–12185	−0.032 to −0.026	0.256–0.853	690.7–691.6	5
113.88	4039–16184	−0.039 to −0.025	0.206–0.956	691.5–695.0	7
132.86	4074–17999	−0.038 to −0.026	0.174–0.908	692.7–699.2	8
151.85	4004–20185	−0.038 to −0.029	0.148–0.892	693.1–704.3	9
170.83	3993–24028	−0.040 to −0.031	0.128–0.944	694.1–711.9	11
189.81	4031–26209	−0.040 to −0.030	0.111–0.928	695.0–721.4	12
208.79	4039–28209	−0.041 to −0.030	0.096–0.927	695.9–731.3	13

where

$$L_{sp,f}/D_h = 1.4039 Re_{sp,f}^{0.25} \delta^{+^{1.25}} \left(1 + 0.1577\delta^{+} - 0.1793\delta^{+^2} - 0.0168\delta^{+^3} + 0.0064\delta^{+^4}\right) \quad \text{for } \delta^{+} < 1. \tag{13}$$

The dimensionless hydrodynamic boundary layer thickness, $\delta^{+}(=\delta/(D_h/2))$, is determined by solving Eq. (13), but, where the flow becomes fully-developed, δ^{+} is set equal to unity, which reduces Eqs. (12) and (13), respectively, to

$$f_{app} = \left(0.07 + 0.316 \frac{L_{sp,f}/D_h}{Re_{sp,f}^{0.25}}\right) \frac{0.25}{L_{sp,f}/D_h} \tag{14}$$

and

$$L_{sp,f}/D_h = 1.3590 Re_{sp,f}^{0.25}. \tag{15}$$

As for the two-phase region, $\Delta p_{tp,G} = 0$ for horizontal flow, and the two-phase pressure drop is composed of only frictional and accelerational components,

$$\Delta p_{tp} = \Delta p_{tp,F} + \Delta p_{tp,A} = \int_0^{L_{tp}} \left[-\left(\frac{dp}{dz}\right)_{tp}\right] dz = \int_0^{L_{tp}} \left[-\left(\frac{dp}{dz}\right)_F - \left(\frac{dp}{dz}\right)_A\right] dz. \tag{16}$$

The integration in Eq. (16) is performed along the flow direction using the one-dimensional finite difference method from the location where $x_e = 0$ to the micro-channel outlet, since $x_{e,out} < 1$ for the present study. The two-phase pressure gradient, $-(dp/dz)_{tp}$, can be determined using one of two models, the Homogeneous Equilibrium Model (HEM) and the Separated Flow Model (SFM), details of which will be addressed in the following sections.

3.2. Two-phase pressure drop

3.2.1. Homogeneous Equilibrium Model (HEM)

The Homogeneous Equilibrium Model treats the two-phase mixture as a pseudo fluid that obeys simple single-phase conservation relations, with the two-phase mixture properties evaluated using appropriate averaging techniques. Three key assumptions of HEM are: (a) velocity profile across each phase is uniform and velocities of the two phases are equal, (b) pressure is uniform across the flow area, and (c) mixture properties are uniform across the flow area.

With a slip ratio of vapor velocity to liquid velocity equal to unity, the mixture density, given by

$$\frac{1}{\bar{\rho}} = \frac{1}{\alpha\rho_g + (1-\alpha)\rho_f} = x_e v_g + (1-x_e) v_f = \bar{v}, \tag{17}$$

provides a simple relationship between void fraction, α, and thermodynamic equilibrium quality, x_e,

$$\alpha = \left[1 + \left(\frac{\rho_g}{\rho_f}\right)\left(\frac{1-x_e}{x_e}\right)\right]^{-1}. \tag{18}$$

The momentum conservation equation for two-phase flow along a uniformly heated channel can be expressed as [44]

$$-\left(\frac{dp}{dz}\right) = \frac{\frac{\tau_F P_F}{A} + G^2 v_{fg} \frac{dx_e}{dz}}{1 + G^2\left[x_e \frac{dv_g}{dp} + (1-x_e)\frac{dv_f}{dp}\right]}, \tag{19}$$

where τ_F, P_F, and A, are, respectively, the frictional shear stress, friction perimeter, and flow area. The frictional shear stress can be expressed as

$$\tau_F = \frac{1}{2}\frac{G^2}{\bar{\rho}} f_{tp} = \frac{1}{2} G^2 f_{tp}[x_e v_g + (1-x_e) v_f], \tag{20}$$

where f_{tp} is the two-phase friction coefficient.

The energy conservation equation is expressed as [44]

$$\frac{dx_e}{dz} = \frac{1}{\left\{h_{fg} + G^2 v_{fg}[x_e v_g + (1-x_e) v_f]\right\}} \times \left\{\frac{q''_H P_H}{GA} - \left[x_e \frac{dh_g}{dp} + (1-x_e)\frac{dh_f}{dp}\right]\frac{dp}{dz} - G^2[x_e v_g + (1-x_e) v_f] \times \left[x_e \frac{dv_g}{dp} + (1-x_e)\frac{dv_f}{dp}\right]\frac{dp}{dz}\right\}, \tag{21}$$

where q''_H is the heat flux applied to the heated perimeter, P_H, of the channel.

Eqs. (19) and (21) are ordinary differential equations that can be combined to yield the following relation for two-phase pressure gradient [44],

$$-\left(\frac{dp}{dz}\right) = \frac{\left\{1 + \frac{G^2 v_{fg}}{h_{fg}}[x_e v_g + (1-x_e) v_f]\right\}\left\{\frac{1}{2} G^2 f_{tp}[x_e v_g + (1-x_e) v_f]\right\}\frac{P_F}{A} + G^2 v_{fg}\left(\frac{q''_H P_H}{GA h_{fg}}\right)}{\left\{1 + \frac{G^2 v_{fg}}{h_{fg}}[x_e v_g + (1-x_e) v_f]\right\} + G^2\left[x_e \frac{dv_g}{dp} + (1-x_e)\frac{dv_f}{dp}\right] - \frac{G^2 v_{fg}}{h_{fg}}\left[x_e \frac{dh_g}{dp} + (1-x_e)\frac{dh_f}{dp}\right]}, \tag{22}$$

which can solved by marching along the axial direction using the Runge-Kutta method. The two terms in the numerator of Eq. (22) represent contributions of friction and acceleration, respectively. And the three terms in the denominator represent, in order, kinetic energy, compressibility, and flashing effects. The compressibility effects are reflected in specific volume gradients with respect to pressure, dv_k/dp ($k = g$ for vapor and f for liquid), and the flashing effects by enthalpy gradients with respect to pressure, dh_k/dp. The quality is then determined by integrating the expression for dx_e/dz given by Eq. (21).

The two-phase friction factor, f_{tp}, for circular tubes is a function of the two-phase mixture Reynolds number, $Re_{tp} = GD_h/\mu_{tp}$, where μ_{tp} is the two-phase mixture viscosity [45],

Table 4
Two-phase mixture viscosity models employed in conjunction with the Homogeneous Equilibrium Model (HEM).

Author(s)	Mixture viscosity
McAdams et al. [46]	$\frac{1}{\mu_{tp}} = \frac{x_e}{\mu_g} + \frac{1-x_e}{\mu_f}$
Akers et al. [47]	$\mu_{tp} = \frac{\mu_f}{\left[(1-x_e) + x_e\left(\frac{v_g}{v_f}\right)^{0.5}\right]}$
Cicchitti et al. [48]	$\mu_{tp} = x_e\mu_g + (1-x_e)\mu_f$
Dukler et al. [49,50]	$\mu_{tp} = \frac{x_e v_g \mu_g + (1-x_e) v_f \mu_f}{x_e v_g + (1-x_e) v_f}$
Beattie & Whalley [51]	$\mu_{tp} = \omega\mu_g + (1-\omega)(1+2.5\omega)\mu_f$ $\omega = \frac{x_e\ v_g}{v_f + x_e\ v_{fg}}$
Lin et al. [52]	$\mu_{tp} = \frac{\mu_f \mu_g}{\mu_g + x_e^{1.4}(\mu_f - \mu_g)}$

Table 5
Correlations for two-phase frictional pressure gradient.

Author(s)	Equation(s)	MAE (%)
Macro-channels		
Lockhart & Martinelli [53]	$\left(\frac{dp}{dz}\right)_F = \left(\frac{dp}{dz}\right)_f \phi_f^2, \phi_f^2 = 1 + \frac{C}{X} + \frac{1}{X^2}, X^2 = \frac{(dp/dz)_f}{(dp/dz)_g}$ $C_{vv} = 5, C_{tv} = 10, C_{vt} = 12, C_{tt} = 20$	87.22
Chisholm [58]	$\left(\frac{dp}{dz}\right)_F = \left(\frac{dp}{dz}\right)_{fo} \phi_{fo}^2, \phi_{fo}^2 = \left[1 + (\Gamma^2 - 1)(Bx_e^{\left(\frac{2-k}{2}\right)}(1-x_e)^{\left(\frac{2-k}{2}\right)} + x_e^{2-k})\right]^{0.5}$ $\Gamma = \left(\left(\frac{f_{go}}{f_{fo}}\right)\left(\frac{\rho_f}{\rho_g}\right)\right)^{0.5}$, $k = 1$ for $Re_{fo} < 2000, 0.25$ for $2000 \leqslant Re_{fo} < 20000, 0.2$ for $Re_{fo} > 20000$ details of parameter B are available in [58]	377.11
Friedel [59]	$\left(\frac{dp}{dz}\right)_F = \left(\frac{dp}{dz}\right)_{fo} \phi_{fo}^2$ $\phi_{fo}^2 = (1-x_e)^2 + x_e^2\left(\frac{v_g}{v_f}\right)\left(\frac{f_{go}}{f_{fo}}\right) + 3.24x_e^{0.78}(1-x_e)^{0.224}\left(\frac{v_g}{v_f}\right)^{0.91}\left(\frac{\mu_g}{\mu_f}\right)^{0.19}\left(1 - \frac{\mu_g}{\mu_f}\right)^{0.7} Fr_{tp}^{-0.045} We_{tp}^{-0.035}$ $Fr_{tp} = \frac{G^2}{gD_h\rho_H^2}, We_{tp} = \frac{G^2 D_h}{\sigma\rho_H}, \rho_H = \frac{1}{x_e v_g + (1-x_e)v_f}$	100.64
Müller-Steinhagen & Heck [60]	$\left(\frac{dp}{dz}\right)_F = \left\{\left(\frac{dp}{dz}\right)_{fo} + 2\left[\left(\frac{dp}{dz}\right)_{go} - \left(\frac{dp}{dz}\right)_{fo}\right]x_e\right\}(1-x_e)^{1/3} + \left(\frac{dp}{dz}\right)_{go} x_e^3$	24.99
Mini/micro-channels		
Mishima & Hibiki [61]	$\left(\frac{dp}{dz}\right)_F = \left(\frac{dp}{dz}\right)_f \phi_f^2, \phi_f^2 = 1 + \frac{C}{X} + \frac{1}{X^2},$ For rectangular channel, $C = 21[1 - \exp(-0.319 \times 10^3 D_h)];\ D_h(\text{m})$ For circular channel, $C = 21[1 - \exp(-0.333 \times 10^3 D)];\ D\ (\text{m})$	27.54
Tran et al. [62]	$\left(\frac{dp}{dz}\right)_F = \left(\frac{dp}{dz}\right)_{fo} \phi_{fo}^2, N_{conf} = \sqrt{\frac{\sigma}{g(\rho_f - \rho_g)D_h^2}} \left(= \sqrt{\frac{1}{Bd}}\right)$ $\phi_{fo}^2 = 1 + \left[4.3\frac{(dp/dz)_{go}}{(dp/dz)_{fo}} - 1\right][N_{conf} x_e^{0.875}(1-x_e)^{0.875} + x_e^{1.75}]$	192.72
Lee & Lee [63]	$\left(\frac{dp}{dz}\right)_F = \left(\frac{dp}{dz}\right)_f \phi_f^2, \phi_f^2 = 1 + \frac{C}{X} + \frac{1}{X^2}, \psi = \frac{\mu_f j_f}{\sigma}, \lambda = \frac{\mu_f^2}{\rho_f \sigma D_h}$ $C_{vv} = 6.833 \times 10^{-8}\lambda^{-1.317}\psi^{0.719} Re_{fo}^{0.557}, C_{tv} = 3.627 Re_{fo}^{0.174}$ $C_{vt} = 6.185 \times 10^{-2} Re_{fo}^{0.726}, C_{tt} = 0.048 Re_{fo}^{0.451}$	40.31
Qu & Mudawar [64]	$\left(\frac{dp}{dz}\right)_F = \left(\frac{dp}{dz}\right)_f \phi_f^2, \phi_f^2 = 1 + \frac{C}{X} + \frac{1}{X^2}$ $C = 21[1 - \exp(-0.319 \times 10^3 D_h)](0.00418G + 0.0613)$	6.66
Sun & Mishima [65]	For $Re_f < 2000$ and $Re_g < 2000$, $\left(\frac{dp}{dz}\right)_F = \left(\frac{dp}{dz}\right)_f \phi_f^2, \quad \phi_f^2 = 1 + \frac{C}{X} + \frac{1}{X^2}, \quad C = 26\left(1 + \frac{Re_f}{1000}\right)\left[1 - \exp\left(\frac{-0.153}{0.27N_{conf} + 0.8}\right)\right]$ For $Re_f \geqslant 2000$ or $Re_g \geqslant 2000$, $\left(\frac{dp}{dz}\right)_F = \left(\frac{dp}{dz}\right)_f \phi_f^2, \quad \phi_f^2 = 1 + \frac{C}{X^{1.19}} + \frac{1}{X^2}, \quad C = 1.79\left(\frac{Re_g}{Re_f}\right)^{0.4}\left(\frac{1-x_e}{x_e}\right)^{0.5}$	35.17
Zhang et al. [66]	$\left(\frac{dp}{dz}\right)_F = \left(\frac{dp}{dz}\right)_f \phi_f^2, \quad \phi_f^2 = 1 + \frac{C}{X} + \frac{1}{X^2}, \quad C = 21[1 - \exp(-0.142/N_{conf})]$	17.56
Kim & Mudawar [57]	$\left(\frac{dp}{dz}\right)_F = \left(\frac{dp}{dz}\right)_f \phi_f^2, \quad \phi_f^2 = 1 + \frac{C}{X} + \frac{1}{X^2}, \quad X^2 = \frac{(dp/dz)_f}{(dp/dz)_g}$ $-\left(\frac{dp}{dz}\right)_f = \frac{2f_f v_f G^2(1-x)^2}{D_h}, -\left(\frac{dp}{dz}\right)_g = \frac{2f_g v_g G^2 x^2}{D_h}$ $f_k = 16Re_k^{-1}$ for $Re_k < 2000$ $f_k = 0.079Re_k^{-0.25}$ *for* $2000 \leqslant Re_k < 20,000$ $f_k = 0.046Re_k^{-0.2}$ *for* $Re_k \geqslant 20,000$ For laminar flow in rectangular channel, $f_k Re_k = 24(1 - 1.3553\beta + 1.9467\beta^2 - 1.7012\beta^3 + 0.9564\beta^4 - 0.2537\beta^5)$ *for* $Re_k < 2000$ where subscript k denotes f or g for liquid and vapor phases, respectively $Re_f = \frac{G(1-x)D_h}{\mu_f}, Re_g = \frac{GxD_h}{\mu_g}, Re_{fo} = \frac{GD_h}{\mu_f}, Su_{go} = \frac{\rho_g \sigma D_h}{\mu_g^2}, We_{fo} = \frac{G^2 D_h}{\rho_f \sigma}, Bo = \frac{q''_H}{Gh_{fg}}$ $C_{non-boiling}: 0.39Re_{fo}^{0.03} Su_{go}^{0.1}\left(\frac{\rho_f}{\rho_g}\right)^{0.35}, 0.39Re_{fo}^{0.03} Su_{go}^{0.1}\left(\frac{\rho_f}{\rho_g}\right)^{0.35}$ $C_{non-boiling}: 8.7 \times 10^{-4} Re_{fo}^{0.17} Su_{go}^{0.50}\left(\frac{\rho_f}{\rho_g}\right)^{0.14}, Re_f \geqslant 2000, Re_g < 2000\ (tv)$ $C_{non-boiling}: 0.0015Re_{fo}^{0.59} Su_{go}^{0.19}\left(\frac{\rho_f}{\rho_g}\right)^{0.36}, Re_f < 2000, Re_g \geqslant 2000\ (vt)$ $C_{non-boiling}: 3.5 \times 10^{-5} Re_{fo}^{0.44} Su_{go}^{0.50}\left(\frac{\rho_f}{\rho_g}\right)^{0.48}, Re_f < 2000, Re_g < 2000\ (vv)$ $C: C_{non-boiling}\left[1 + 60We_{fo}^{0.32}\left(Bo\frac{P_H}{P_F}\right)^{0.78}\right], Re_f \geqslant 2000$ $C: C_{non-boiling}\left[1 + 530We_{fo}^{0.52}\left(Bo\frac{P_H}{P_F}\right)^{1.09}\right], Re_f < 2000$	14.56

$$f_{tp} = 16Re_{tp}^{-1} \text{ for } Re_{tp} < 2000, \tag{23}$$

$$f_{tp} = 0.079Re_{tp}^{-0.25} \text{for } 2000 \leqslant Re_{tp} < 20,000, \tag{24}$$

and

$$f_{tp} = 0.046Re_{tp}^{-0.2} \text{for } Re_{tp} \geqslant 20,000. \tag{25}$$

For laminar flow in a rectangular channel, Eq. (23) must be replaced by [40]

$$f_{tp} = \frac{24}{Re_{tp}}(1 - 1.3553\beta + 1.9467\beta^2 - 1.7012\beta^3 + 0.9564\beta^4 - 0.2537\beta^5) \text{ for } Re_{tp} < 2000. \tag{26}$$

Table 6
Application ranges of SFM two-phase frictional pressure gradient correlations.

Authors(s)	Diameter	Adiabatic/ boiling	Fluid(s)	Configuration	Remarks
Macro-channels					
Lockhart & Martinelli [53]	D_h = 1.49–25.83 mm	Adiabatic	Water, oils, benzene, kerosene	C, H/V (various angles), single channel	Low pressure: p =110–360 kPa
Chisholm [58]	N/A	Boiling	Water, R22, liquid metals	C, H, single channel	Turbulent-turbulent flow
Friedel [59]	D_h > 4 mm	Adiabatic	Air-water, air-oil, R12	R/C/ANN, H/VU/VD	Mostly circular tube data, 25,000 data points
Muller-Steinhagen & Heck [60]	D_h = 4–392 mm	Adiabatic	Air-water, air-oil, argon, argon-ethanol, argon-water, steam-water, hydrocarbons, neon, nitrogen, R11, R12, R12	R/C, H/VU/VD	9300 data points
Mini/micro-channels					
Mishima & Hibiki [61]	D_h = 0.7–25.37 mm	Adiabatic	Air-water, Ammonia, R113-N2	R/C, VU/H, single channel	
Tran et al. [62]	Circular: D = 2.46, 2.92 mm rectangular: D_h = 2.40 mm	Boiling	R134a, R12, R113	R/C, H, single channel	p = 138–856 kPa, p_r = 0.04–0.23, 610 data points
Lee & Lee [63]	D_h = 0.78, 1.91, 3.64, 6.67 H_{ch} = 0.4, 1, 2, 4 mm W_{ch} = 20 mm	Adiabatic	Air-water	R, H, single channel	water: j_f = 0.03–2.39 m/s air: j_g = 0.05–18.7 m/s X = 0.303–79.4, Re_{fo} = 175–17700, 305 data points
Qu & Mudawar [64]	D_h = 348.9 µm W_{ch} = 231 µm, H_{ch} = 713 µm	Boiling	Water	R, H, multi-channel	21-channel heat sink
Sun & Mishima [65]	D_h = 0.506–12 mm	Adiabatic/ boiling/ condensing	Adiabatic: air-water, R134a, R22, R236ea, R245fa, R407C, R410a boiling: water, CO_2, R123, R134a, R22, R402a, R404a, R407C, R410A, R502, R507 condensing: R134a	R/C/Semi-triangular/ ANN, single channel, multi-channel	Re_f = 10–37000, Re_g = 3–4 × 10^5, 1840 data points
Zhang et al. [66]	D_h = 0.07–6.25 mm	Adiabatic/ boiling	Adiabatic: air-water, N_2-water, air-ethanol, air-oil, NH_3, N_2-R113, R134a, R22, R236ea, R404a, R410A boiling: water, R134a, R12	R/C, H/VU, single channel, multi channel	2201 data points
Kim & Mudawar [57]	D_h = 0.349–5.35 mm	Boiling	Water, R12, R134a, CO_2, R410A, R22, R245fa, FC72, ammonia	R/C, H/VU, single channel, multi-channel	Re_{fo} = 156–28010, p_r = 0.005–0.78, 2378 data points

C: circular, R: rectangular, ANN: annulus, H: horizontal, VU: vertical upwards, VD: vertical downwards.

Notice that the two-phase Reynolds number and two-phase friction factor are functions of the specific mixture viscosity relation employed in HEM. Table 4 provides six popular relations for the mixture viscosity.

3.2.2. Separated Flow Model (SFM) and Slip Flow Model

Unlike HEM, the Separated Flow Models (SFMs) allow for velocity differences between the two phases. While SFMs also allow velocity variations within each phase, the simplest form of the SFM, the Slip Flow Model, assumes uniform velocity profiles within each phase. With a slip ratio of vapor velocity to liquid velocity different from unity, the simple relation between α and x_e employed with HEM, Eq. (18), is not valid for the Slip Flow Model. This is why several alternative relations between α and x_e have been proposed to facilitate closure in implementing momentum and energy conservation when employing this model [53–56]. Despite differences among these relations, they provide fairly similar predictions for the two-phase accelerational pressure gradient for micro-channels [57]. The relation by Zivi [54]

$$\alpha = \left[1 + \left(\frac{\rho_g}{\rho_f}\right)^{2/3}\left(\frac{1-x_e}{x_e}\right)\right]^{-1} \tag{27}$$

is the most popular of these relations and is therefore employed in the present study.

For the Slip Flow Model, the accelerational pressure gradient is given by [57]

$$-\left(\frac{dp}{dz}\right)_A = G^2\frac{d}{dz}\left[v_g\frac{x^2}{\alpha} + v_f\frac{(1-x)^2}{(1-\alpha)^2}\right] = G^2\left\{2\left[v_g\frac{x_e}{\alpha} - v_f\frac{1-x_e}{1-\alpha}\right]\frac{dx_e}{dz} - \left[v_g\frac{x_e^2}{\alpha^2} - v_f\frac{(1-x_e)^2}{(1-\alpha)^2}\right]\frac{d\alpha}{dx_e}\right\} \tag{28}$$

where

$$\frac{d\alpha}{dx_e} = \left(\frac{v_f}{v_g}\right)^{2/3}\frac{1}{\left[x_e + (1-x_e)\left(v_f/v_g\right)^{2/3}\right]^2} \tag{29}$$

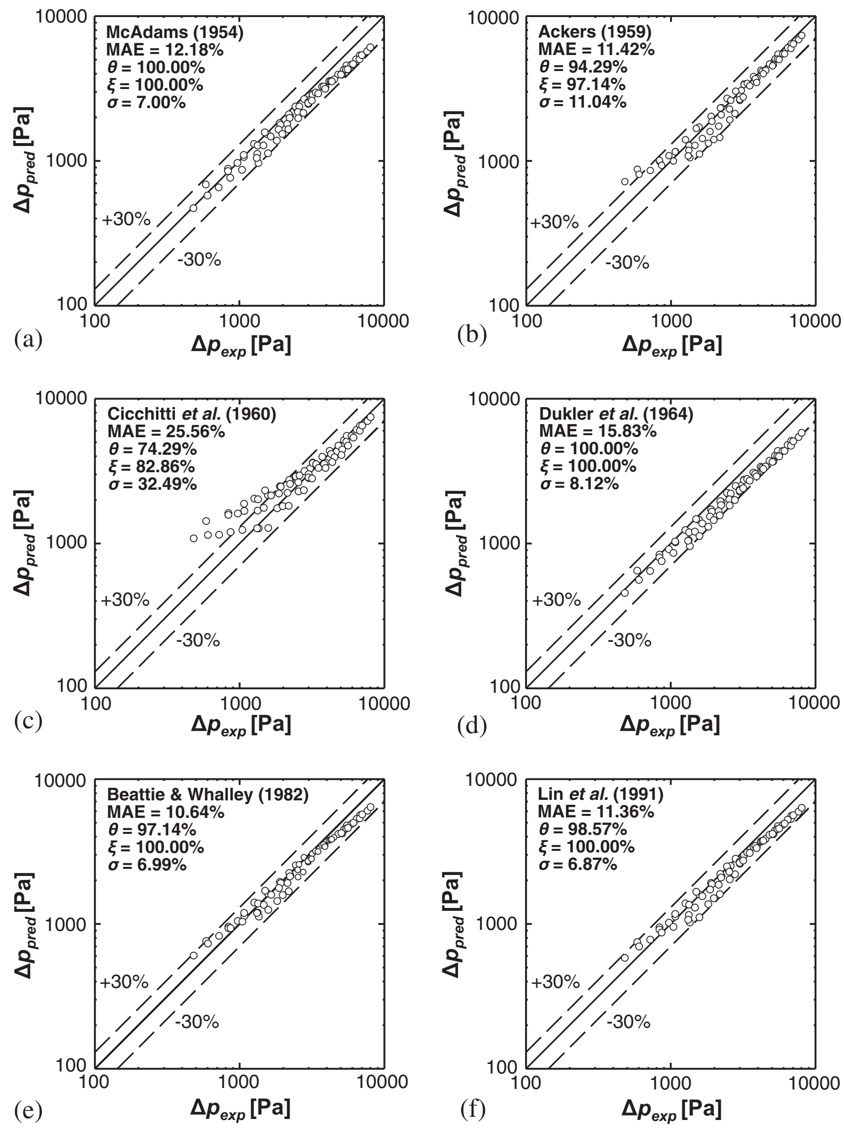

Fig. 4. Comparison of present pressure drop data with predictions of Homogeneous Equilibrium Model using two-phase viscosity models/relations of: (a) McAdams [46], (b) Akers [47], (c) Cicchitti et al. [48], (d) Dukler et al. [49,50], (e) Beattie and Whalley [51], and (f) Lin et al. [52].

and

$$\frac{dx_e}{dz} = \frac{q''_H P_H}{GAh_{fg}}. \tag{30}$$

The frictional pressure gradient is expressed as the product of a friction factor for each phase, f_k, and corresponding two-phase multiplier, ϕ_k^2 [57].

$$\left(\frac{dp}{dz}\right)_F = \left(\frac{dp}{dz}\right)_f \phi_f^2 = \left(\frac{dp}{dz}\right)_g \phi_g^2, \tag{31}$$

where

$$-\left(\frac{dp}{dz}\right)_f = \frac{2f_f v_f G^2 (1-x_e)^2}{D_h} \tag{32}$$

and

$$-\left(\frac{dp}{dz}\right)_g = \frac{2f_g v_g G^2 x_e^2}{D_h}. \tag{33}$$

The friction factors in Eqs. (32) and (33) are given by

$$f_k = 16 Re_k^{-1} \text{ for } \quad Re_k < 2000, \tag{34}$$

$$f_k = 0.079 Re_k^{-0.25} \text{ for } \quad 2000 \leqslant Re_k < 20,000, \tag{35}$$

and

$$f_k = 0.046 Re_k^{-0.2} \text{ for } \quad Re_k \geqslant 20,000, \tag{36}$$

where

$$Re_k = Re_f = \frac{G(1-x_e)D_h}{\mu_f} \text{ for liquid} \tag{37}$$

and

$$Re_k = Re_g = \frac{G x_e D_h}{\mu_g} \text{ for vapor.} \tag{38}$$

For laminar flow in a rectangular channel with Re_k < 2000, the friction factor is obtained by using Eq. (26) after substituting f_k for f_{tp} and Re_k for Re_{tp}.

Table 5 provides a summary of four macro-channel and seven micro-channel SFM correlations for the frictional component of pressure drop that are assessed in this study. Table 6 provides additional details concerning these correlations.

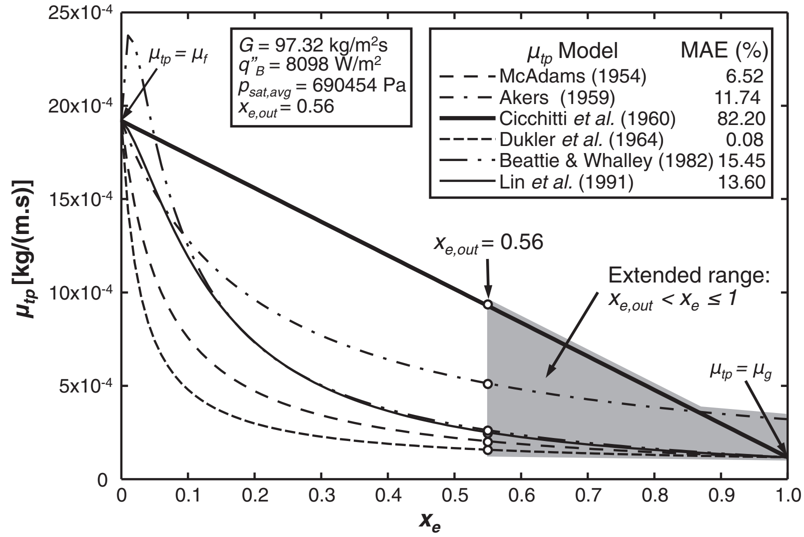

Fig. 5. Variation of two-phase mixture viscosity with thermodynamic equilibrium quality predicted according to different viscosity models adopted in conjunction with the Homogeneous Equilibrium Model.

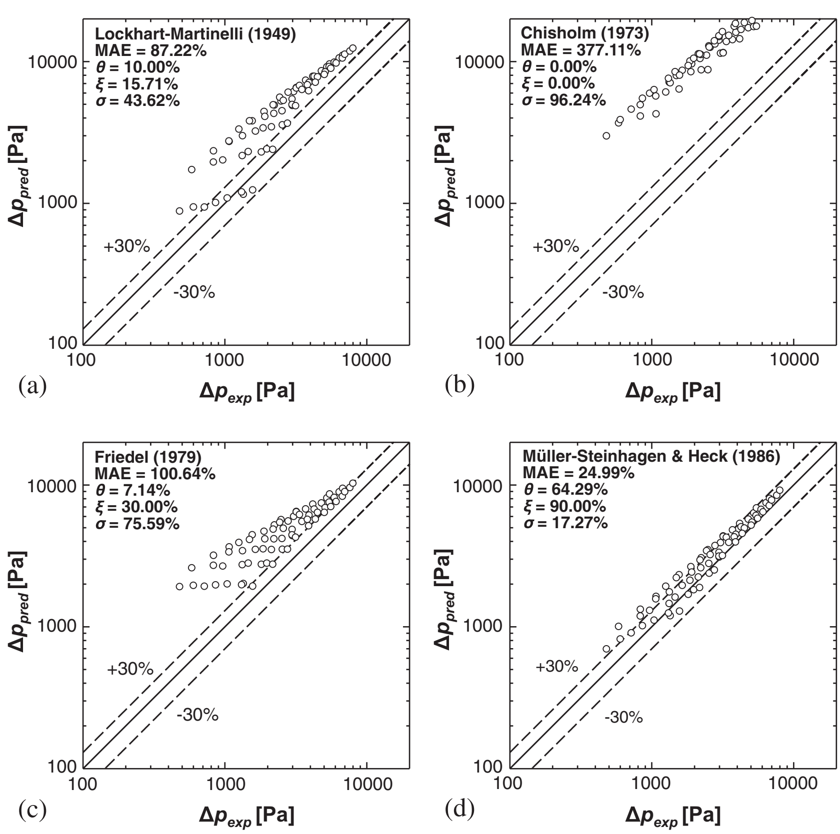

Fig. 6. Comparison of present pressure drop data with predictions of empirical separated flow correlations recommended for macro-channels: (a) Lockhart and Martinelli [53], (b) Chisholm [58], (c) Friedel [59], and (d) Müller-Steinhagen and Heck [60].

4. Assessment of pressure drop predictive methods

4.1. Assessment methodology

The present pressure drop data include not only the two-phase frictional pressure drop, $\Delta p_{tp,F}$, but also the pressure drops associated with two-phase acceleration, $\Delta p_{tp,A}$, inlet contraction, Δp_c, upstream single-phase liquid flow, $\Delta p_{sp,f}$, and outlet recovery, Δp_e. Excepting $\Delta p_{tp,F}$, identical formulations are used to predict all the other pressure drop components as discussed in the previous sections. The accuracy of predictions is quantified with the aid of mean absolute error (MAE), defined as

$$MAE(\%) = \frac{1}{N}\sum\left[\frac{|\Delta p_{pred} - \Delta p_{\exp}|}{\Delta p_{\exp}} \times 100\right]. \quad (39)$$

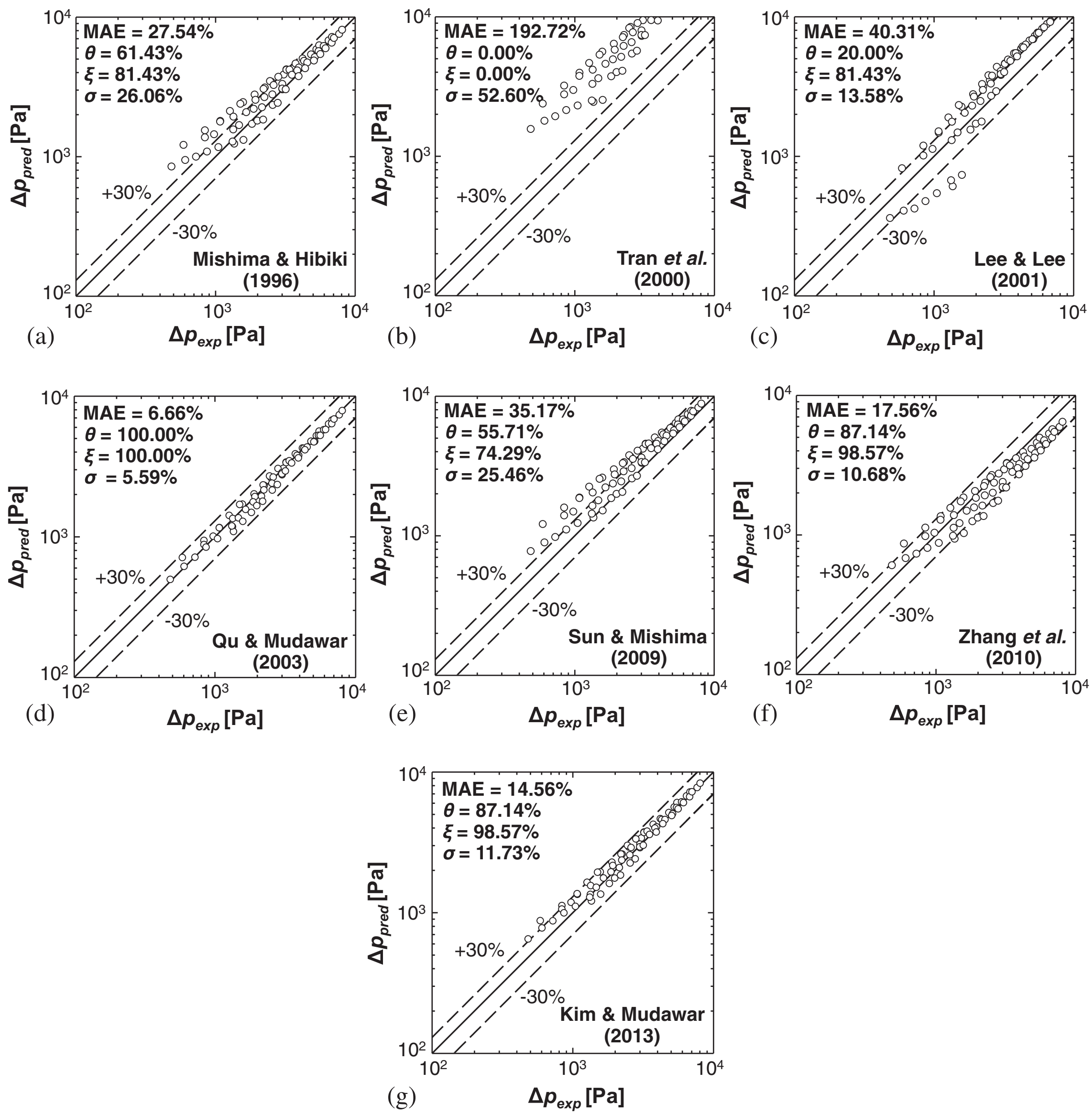

Fig. 7. Comparison of present pressure drop data with predictions of separated flow empirical correlations recommended for micro-channels: (a) Mishima and Hibiki [61], (b) Tran et al. [62], (c) Lee and Lee [63], (d) Qu and Mudawar [64], (e) Sun and Mishima [65], (f) Zhang et al. [66], and (g) and Kim and Mudawar [57].

Predictive accuracy is further assessed by parameters θ and ξ, which are defined as percentages of the data predicted within ±30% and ±50%, respectively, as well as standard deviation, σ, which is defined as

$$\sigma(\%) = \sqrt{\frac{\sum (MAE - MAE_{avg})^2}{(N-1)}}. \tag{40}$$

4.2. Experimental data versus HEM predictions

Fig. 4 compares the present pressure drop data with predictions of HEM using the six two-phase viscosity relations provided in Table 4. Overall, excepting the viscosity relation of Cicchitti et al. [48], Fig. 4(c), all the other viscosity relations show fairly good predictions of the data, evidenced by MAE values below 15.83%, and θ and ξ better than 94.29% and 97.14%, respectively. For the relation of Cicchitti et al., MAE = 25.56%, and θ and ξ are 74.29% and 82.86%, respectively.

The inferior performance of the Cicchitti et al. relation can be explained by examining a particular test corresponding to $q''_B = 8098$ W/m^2 and $G = 97.32$ kg/m^2 s, for which this relation showed a MAE of 82.20% compared to less than 16% for all the other relations. Fig. 5 shows the dependence of the different viscosity relations on thermodynamic equilibrium quality for this particular test, where the liquid and vapor properties are evaluated at the average of the micro-channel inlet and outlet pressures. Excepting the Akers relation [47], all the other viscosity relations satisfy the limiting conditions of $\mu_{tp} = \mu_f$ for $x_e = 0$ and $\mu_{tp} = \mu_g$ for $x_e = 1$, but follow different trends in between. Notice that the relation of Cicchitti's et al. over-predicts mixture viscosity considerably, especially at low qualities, compared to the other relations, resulting in higher values for two-phase friction factor, f_{tp}, which is reflected in higher MAE values for this relation. Interestingly, the relations of McAdams [46] and Dukler et al. [49,50], which provide the lowest estimates for mixture viscosity, also yield the best predictions.

4.3. Experimental data versus predictions of Macro-channel SFM correlations

Fig. 6 compares the present experimental data with predictions of SFM correlations recommended for macro-channels. The

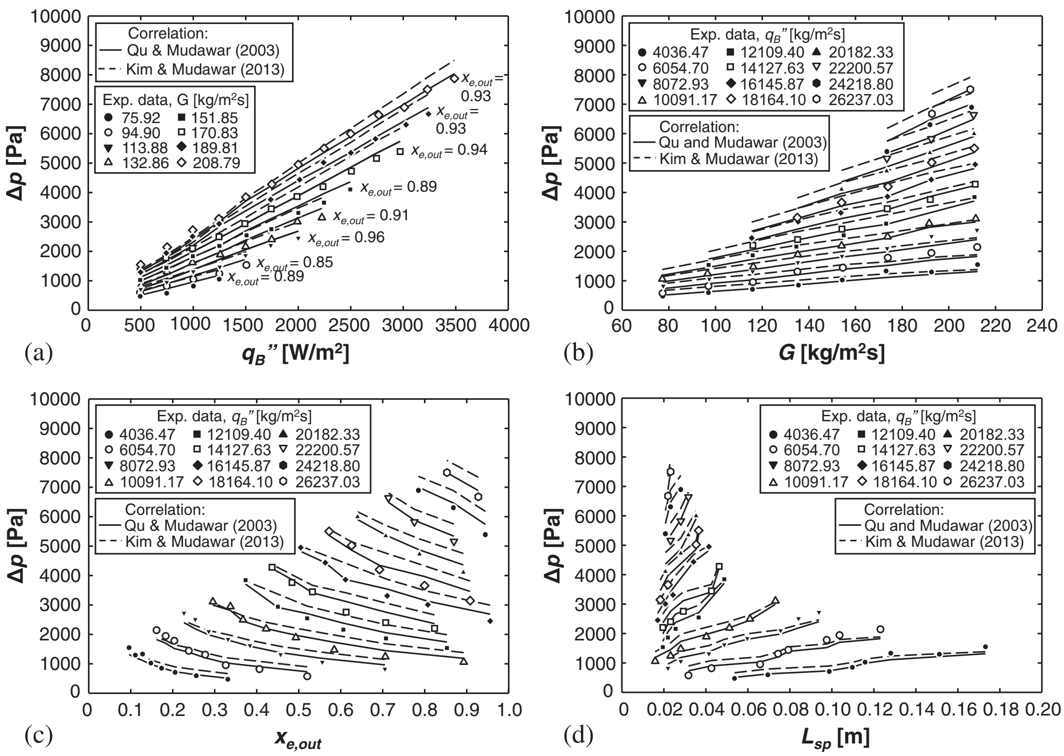

Fig. 8. Variations of pressure drop across micro-channels with (a) heat flux, (b) mas velocity, (c) exit quality, and (d) length of single-phase liquid flow region.

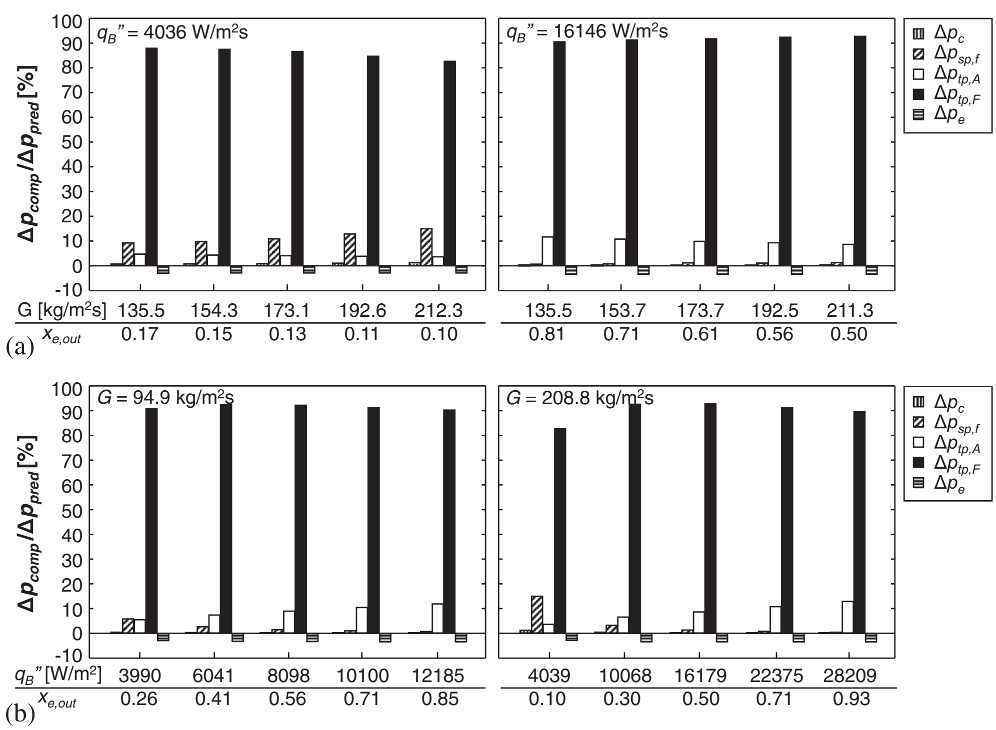

Fig. 9. Contributions of individual pressure drop components to total pressure drop predicted according to Qu and Mudawar's correlation [64] for different operating conditions corresponding to (a) fixed heat flux and (b) fixed mass velocity.

correlations by Lockhart and Martinelli [53], Fig. 6(a), Chisholm [58], Fig. 6(b), and Friedel [59], Fig. 6(c), are shown yielding poor predictions, reflected by MAE values of 87.22%, 377.11%, and 100.64%, respectively. Far better predictions are achieved with the Müller-Steinhagan and Heck correlation [60], Fig. 6(d), which has a MAE of 24.99%. The superior performance of this correlation may be explained by its broad application range, being based on 9300 data points for rectangular and circular channels, including several fluids with drastically different thermophysical properties, and different flow configurations and flow orientations. On the

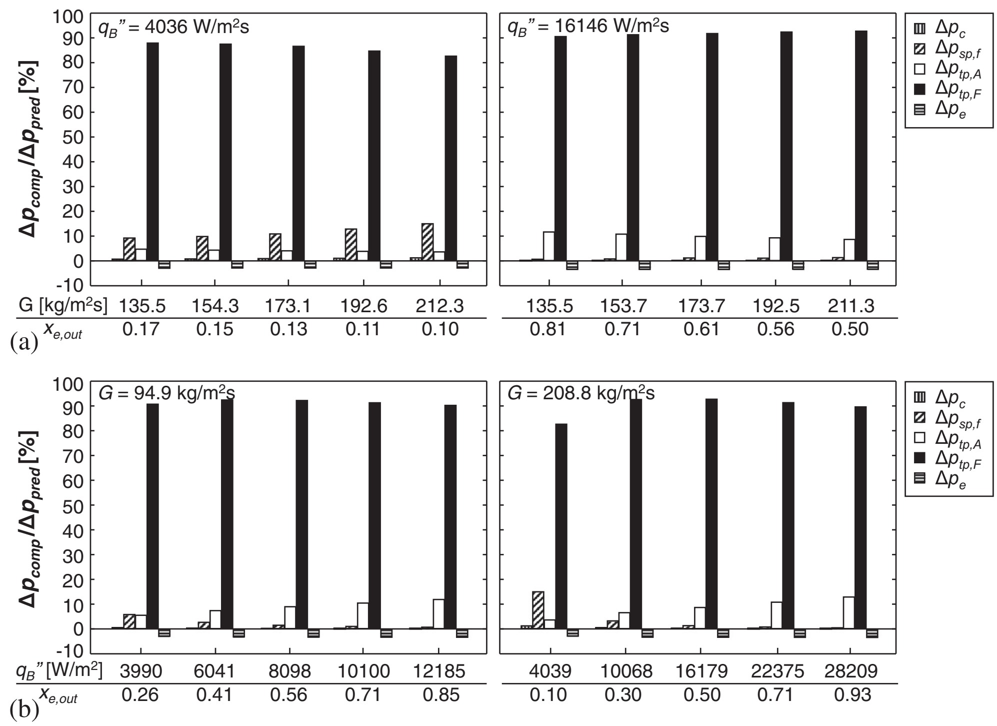

Fig. 10. Contributions of individual pressure drop components to total pressure drop predicted according to Kim and Mudawar's correlation [57] for different operating conditions corresponding to (a) fixed heat flux and (b) fixed mass velocity.

other hand, the Lockhart and Martinelli correlation and Friedel correlation, which greatly over-predict the data, are derived from relatively small databases. And the Chisholm correlation, which shows the highest MAE, is based on adiabatic flow data, but modified for flow boiling at high vapor and liquid (turbulent-turbulent) flow rates.

4.4. Experimental data versus predictions of Micro-channel SFM correlations

Fig. 7 compares the present experimental data with predictions of SFM correlations recommended for mini/micro-channels. Overall, predictions based on these frictional drop correlations are far better than those for macro-channels, Fig. 6. Interestingly, the Mishima and Hibiki correlation [61], Fig. 7(a), shows fair agreement (MAE = 27.54%) despite being based on adiabatic flow data. Of the seven micro-channel correlations examined in Fig. 7, the one by Tran et al. [62], Fig. 7(b), shows the highest MAE of 192.72%. A unique feature of the Tran et al. correlation is its use of the liquid-only pressure gradient, $(dp/dz)_{fo}$, and liquid-only multiplier, ϕ_{fo}, while all the others are based on $(dp/dz)_f$ and ϕ_f, where $\phi_f^2 = 1 + C/X + 1/X^2$. The Lee and Lee correlation [63], which, like Mishima and Hibiki's, is based on adiabatic flow data, but high aspect ratio channels, shows a higher MAE of 40.31%, Fig. 7(c). And, while Qu and Mudawar's correlation [64] employs a formulation similar to that of Mishima and Hibiki, its reliance on data for flow boiling with subcooled inlet conditions in a multi rectangular channel heat sink, conditions similar to those of the present study, shows the best overall predictive accuracy with a MAE of 6.66%, Fig. 7(d). The remaining three correlations by Sun and Mishima [65], Zhang et al. [66], and Kim and Mudawar [57], are each based on a very large database and a variety of fluids and flow configurations. Among the three, better accuracy is achieved using the correlation of Kim and Mudawar, Fig. 7(g), followed by Zhang et al., Fig. 7(f), and Sun and Mishima, Fig. 7(e), with MAE values of 14.56%, 17.56%, and 35.17%, respectively.

4.5. Dominant component of pressure drop

Further insight into the pressure drop characteristics is achieved by examining the variations of pressure drop relative to key parameters, as well as the contributions of individual pressure drop components to total pressure drop. This is accomplished by examining predictions based on the correlations of Qu and Mudawar [64] and Kim and Mudawar [57], which, as shown in Fig. 7, yielded the lowest MAE of the seven micro-channel correlations tested, 6.66% and 14.56%, respectively.

Fig. 8 shows parametric variations of measured pressure drop as well as pressure drop predicted according to the Qu and Mudawar and Kim and Mudawar correlations. Shown are pressure drop variations relative to heat flux, Fig. 8(a), mass velocity, Fig. 8(b), exit quality, Fig. 8(c), and single-phase length, Fig. 8(d). In each case, remarkable agreement is achieved between the data and predicted trends for both correlations.

Fig. 8(a) shows pressure drop increases monotonically with increasing heat flux, q''_B, but with a slope that increases with increasing G. For fixed q''_B, Fig. 8(b) shows pressure drop increases linearly with increasing G, with a slope that also increases with increasing q''_B. The increases relative to q''_B and G are primarily the result of increasing frictional pressure drop brought about by increases in mean velocity of the two-phase mixture. Increasing q''_B also increases the fraction of the micro-channel length undergoing flow boiling. Fig. 8(c) shows Δp increasing monotonically with increasing q''_B. It should be emphasized that the counterintuitive decrease in Δp with increasing x_e for a given heat flux is in fact the result of decreasing G. Fig. 8(d) shows longer upstream single-phase liquid length, L_{sp}, is achieved at high G and small q''_B. The same figure shows L_{sp} decreases and Δp increases with increasing q''_B. Here too, the increase in Δp with increasing L_{sp} is the result of increasing G.

Figs. 9 and 10 show the percentage contributions of individual pressure drop components to total pressure drop predicted according to the correlations of Qu and Mudawar [64] and Kim and

(a)
(b)

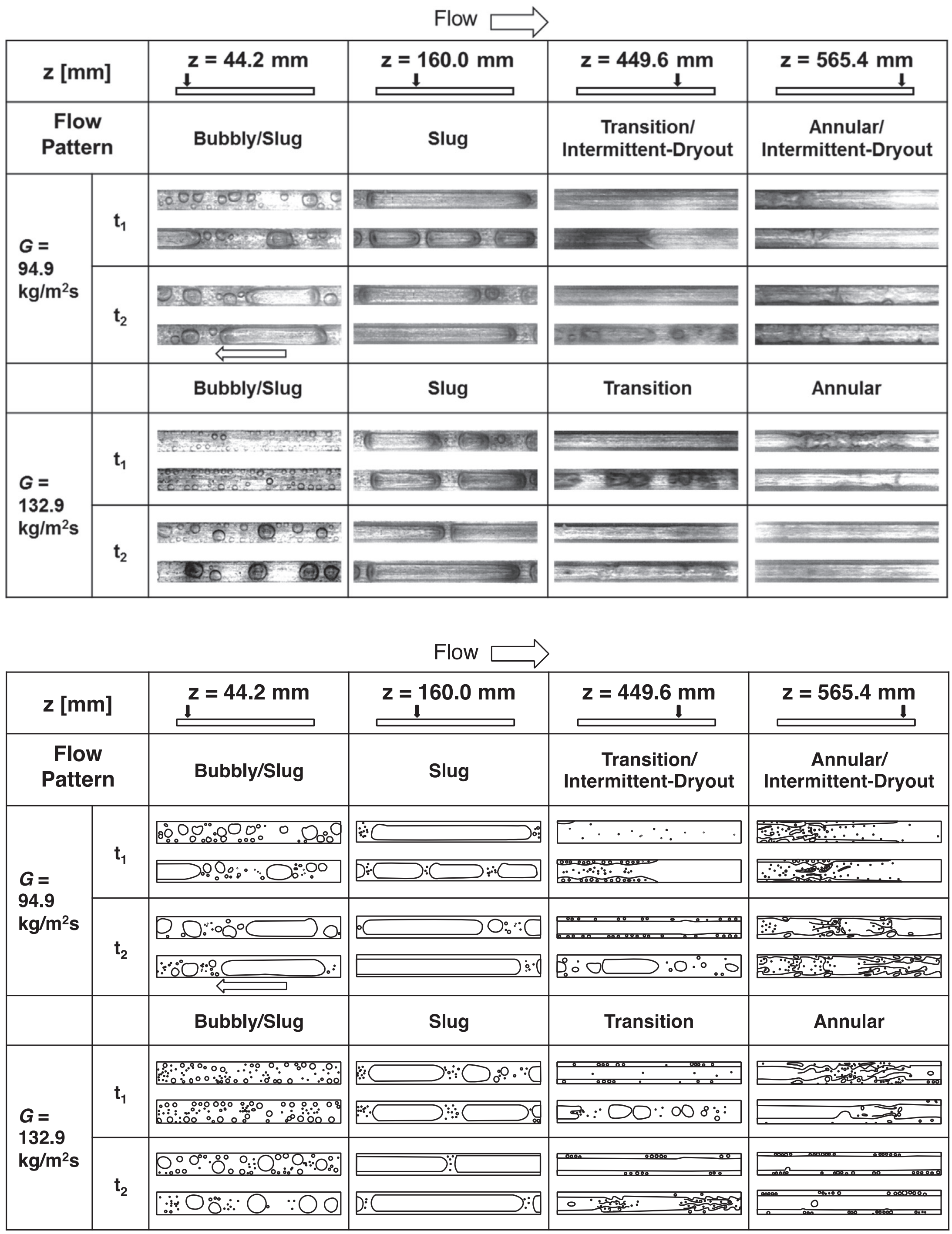

Fig. 11. Representative (a) photographs and (b) schematics of R-134a transient flow boiling patterns at four axial locations along micro-channel heat sink at two different times, t_1 and t_2, for $q''_B = 12{,}109$ W/m^2 and $G = 94.9$ and 132.9 kg/m^2 s.

Mudawar [57], respectively. In each case, the variations of component percentages are presented against G and q''_B. Overall, these plots show pressure drop is dominated overwhelmingly by two-phase friction ($\Delta p_{tp,F}$). Figs. 9(a) and 10(a) show the percentage contributions of pressure drop components versus G for two heat fluxes, $q''_B = 4036$ and $16{,}146$ W/m^2 s. Notice how the percentage contribution of two-phase acceleration ($\Delta p_{tp,A}$) is quite small for $q''_B = 4036$ W/m^2 s and more noticeable for $q''_B = 16{,}146$ W/m^2 s. For the lower heat flux, the $\Delta p_{tp,F}$ percentage is shown decreasing with increasing G, while, for the higher heat flux, the percentage contribution of $\Delta p_{tp,F}$ increases slightly and $\Delta p_{tp,A}$ decreases with increasing G.

Figs. 9(b) and 10(b) show the percentage contributions of pressure drop components versus q''_B for two mass velocities, $G = 94.9$ and 208.8 kg/m^2 s. Both figures show the $\Delta p_{tp,A}$ percentage increasing and $\Delta p_{sp,f}$ mostly decreasing with increasing q''_B as L_{sp} decreases. The decrease in the $\Delta p_{sp,f}$ percentage is also a bit more pronounced for $G = 208.8$ kg/m^2 s compared to 94.9 kg/m^2 s.

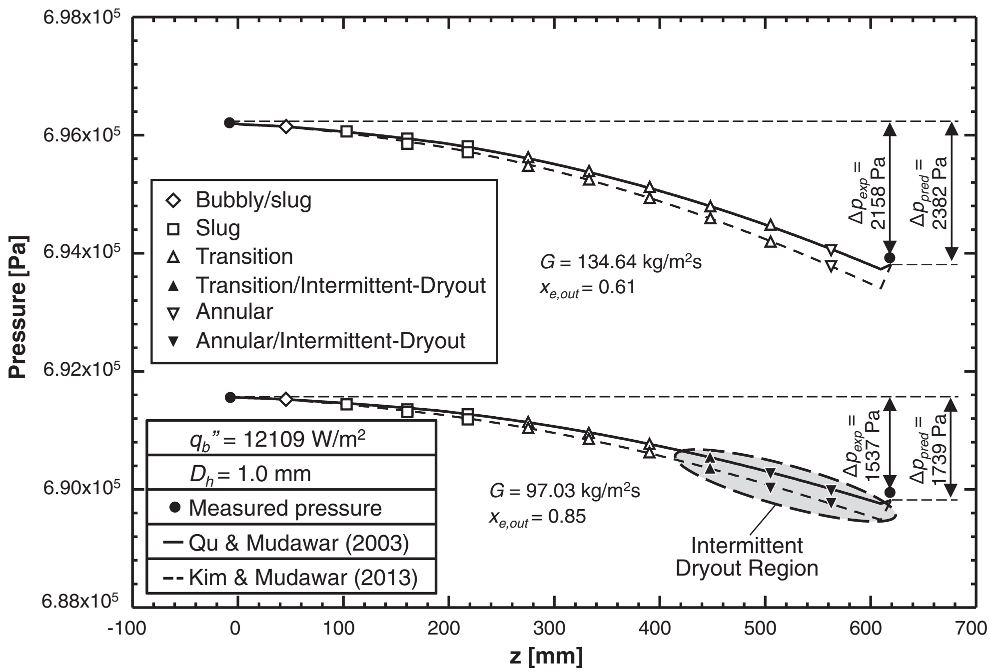

Fig. 12. Pressure variations along micro-channel heat sink predicted according to Qu and Mudawar [62] and Kim and Mudawar [44], along with observed local flow patterns for q''_B = 12,109 W/m^2 with G = 97.03 and 134.64 kg/m^2 s.

5. Flow visualization of interfacial behavior and flow patterns

Notice that, in addition to the parameters discussed earlier, pressure drop is influenced by interfacial behavior and dominant flow patterns. To better understand boiling behavior along the micro-channels, high-speed video imaging is used to capture interfacial behavior and flow patterns in two adjacent micro-channels, as well as transient fluctuations, at four axial locations and mass velocities of G = 94.9 and 132.9 kg/m^2 s. Fig. 11(a) shows representative flow images, while corresponding schematics are depicted in Fig. 11(b). For each mass velocity and axial location, two different images are provided for two different times, t_1 and t_2, corresponding to instants of highest and lowest liquid content in one cycle of the periodic flow pattern fluctuations as suggested in a previous study by the authors [35]. It is important to note that the ability to identify dominant flow patterns during flow pattern fluctuations is, at times, hindered by high complexity of interfacial structures, especially near flow pattern boundaries. Four primary flow patterns are identified: *bubbly/slug*, *slug*, *transition* and *annular*, along with two other patterns associated specifically with downstream dryout: *transition* and *annular*. Observed in subcooled and low quality saturated boiling regions, *bubbly/slug flow* fluctuates between *bubbly flow*, consisting of a large number of smaller bubbles, and *slug flow*, where small bubbles coalesce into large oblong bubbles separated by liquid slugs containing small bubbles. *Bubbly flow* alone and *slug flow* alone are observed mostly upstream during the ‘liquid surge period’ and ‘liquid deficient period’, respectively. The *bubbly/slug flow* is associated mostly with *backflow*, where the elongated bubbles move upstream, except for high G and low q''_B conditions. The elongated bubble shape is inverted as it moves backwards as indicated for time t_2 corresponding to z = 44.2 mm and G = 94.9 kg/m^2 s. The ensuing *slug flow* features a series of liquid slugs and elongated bubbles, with velocities rapidly increasing along the channel with the increasing void fraction. Additionally, bubble nucleation along the wall within the liquid slugs is significantly subdued as the liquid slug's temperature approaches saturation temperature, with the phase change continuing to occur mostly at the boundary between the liquid slug and elongated bubble. Downstream, *slug flow* is replaced by *transition flow*, which consists of periodic fluctuations between *slug flow* and *annular flow*. As shown for time t_2 corresponding to z = 449.6 mm and G = 132.9 kg/m^2 s, liquid droplets are formed mostly by full breakup of remaining liquid slugs from the upstream *slug flow* and to a lesser extent by interfacial breakup in *annular flow* due to high vapor shear. Qu and Mudawar [64] emphasized the importance of the entrained droplets in their theoretical pressure drop model. *Transition flow* is reminiscent of the *churn/annular flow* pattern described in [67], and associated with locally high heat transfer coefficients [36]. As shown for z = 565.4 mm and G = 94.9 kg/m^2 s, *annular flow* is established at time t_1 and the liquid film is consumed by evaporation before the wall is replenished with a wave-like liquid cluster. *Dryout* occurs when the liquid film's evaporation time is shorter than a half period of the periodic cycle for this condition. Notice that no *dryout* is observed for the same location and heat flux for the higher mass velocity of G = 132.9 kg/m^2 s; bubbles covering the heated wall are washed away and the annular film is re-established at t_1 and t_2, respectively. It is important to note that *dryout* has a noticeable influence on local frictional pressure gradient as the liquid covering the wall is replaced by vapor.

Recent studies addressing flow boiling in heat sinks containing parallel micro-channels describe fluctuations in flow patterns, especially between *slug flow* and *annular flow*, and the ensuing dryout in manner that is more-or-less similar to that observed in the present study. Wang and Bergles [68] described the influence of temporal dryout on the pressure gradient in conjunction with three flow patterns: steady bubbly/slug, alternating bubbly/annular, and alternating annular/mist. Revellin et al. [67] and Thome [69] described alternating slug/semi-annular and semi-annular patterns during the transition from churn-like flow to annular flow. Saitoh et al. [70] pointed to flow instabilities as a key reason for the periodic flows and heat transfer degradation resulting from temporal dryout.

Clearly, the dominant flow patterns and transitions between patterns are closely related to local pressure gradient. To further investigate this relationship, the axial pressure variations predicted according to the correlations of Qu and Mudawar [64] and Kim and Mudawar [57] (including the other pressure drop components) are designated with observed flow patterns corresponding to axial locations of the heat sink thermocouples. Fig. 12 shows these variations for $q''_B = 12{,}109\ \mathrm{W/m^2}$ and two mass velocities, and includes the predicted and measured pressure drops. The MAEs for $G = 97.03\ \mathrm{kg/m^2\,s}$ and $G = 134.64\ \mathrm{kg/m^2\,s}$ are 13.16% and 10.39% for Qu and Mudawar, and 23.27% and 29.29% for Kim and Mudawar, respectively. It should be noted that pressure drop correlation of Qu and Mudawar developed by using annular flow dominant database. Also notice that the pressure gradient is relatively small for *bubbly flow* and *slug flow*, and, because of the axial increases in both flow velocity and two-phase friction, increases appreciably in *transition flow* and *annular flow*.

Clearly, more research is required to address the role of flow instabilities and fluctuations between flow patterns since most two-phase pressure drop correlations and/or models are based on the assumption of a single dominant flow pattern.

6. Conclusions

This study addressed the two-phase pressure drop characteristics of R134a for a heat sink containing large length-to-diameter parallel micro-channels with subcooled inlet conditions. This included detailed pressure drop measurements obtained over broad ranges of mass velocity and heat flux, as well as high-speed video analysis of interfacial behavior and flow patterns. The data were compared to predictions of three types of models: Homogeneous Equilibrium Model (HEM) with different two-phase mixture viscosity relations, correlations based on the Separated Flow Model (SFM) and intended for macro-channels, and correlations based on SFM and intended for micro-channels. Key conclusions from the study are as follows.

(1) Six popular two-phase mixture viscosity relations used in conjunction with HEM showed fairly good accuracy in predicting pressure across the micro-channels, evidenced by MAE values smaller than 16%, excepting the viscosity relation by Cicchitti et al., which had a MAE of 25.56%.
(2) Four different macro-channel correlations based on SFM showed relatively poor overall accuracy in predicting the present pressure drop data. MAE values ranged from 24.99% for the Müller-Steinhagan and Heck correlation to 377.11% for the Chisholm correlation.
(3) Seven different correlations based on SFM and intended specifically for micro-channels showed better overall accuracy than SFM macro-channel correlations. These micro-channel correlations showed MAE values ranging from 6.66% to 59.95%, excepting the correlation of Tran et al., which had a MAE of 192.72%. Highest predictive accuracy was achieved with the correlations of Qu and Mudawar and Kim and Mudawar, which showed MAE values of 6.66% and 14.56%, respectively.
(4) Predictions show that two-phase frictional pressure drop is the most dominant of five components comprising total pressure drop, followed by either the two-phase accelerational or single-phase frictional components, depending on operating conditions.
(5) The flow visualization results show appreciable periodic fluctuations in flow patterns. They consist of four primary patterns: *bubbly/slug*, *slug*, *transition*, and *annular*, along with two other patterns associated specifically with downstream dryout: *transition* and *annular*.

Acknowledgement

The authors are grateful for the support of the National Aeronautics and Space Administration (NASA) under grant NNX13AB01G.

Conflict of interest

The authors declared that there is no conflict of interest.

References

[1] I. Mudawar, Assessment of high-heat-flux thermal management schemes, IEEE Trans. – CPMT 24 (2001) 122–141.
[2] C.L. Tien, K.S. Chung, Entrainment limits in heat pipes, AIAA J. 17 (1979) 643–646.
[3] M. Shafahi, V. Bianco, H. Vafai, O. Manco, An investigation of the thermal performance of cylindrical heat pipes using nanofluids, Int. J. Heat Mass Transf. 53 (2010) 376–383.
[4] T.J. LaClair, I. Mudawar, Thermal transients in a capillary evaporator prior to the initiation of boiling, Int. J. Heat Mass Transf. 43 (2000) 3937–3952.
[5] P.J. Marto, V.J. Lepere, Pool boiling heat transfer from enhanced surfaces to dielectric fluids, J. Heat Transf. 104 (1982) 292–299.
[6] I. Mudawar, T.M. Anderson, Optimization of extended surfaces for high flux chip cooling by pool boiling, J. Electron. Pack. 115 (1993) 89–100.
[7] I. Mudawar, A.H. Howard, C.O. Gersey, An analytical model for near-saturated pool boiling CHF on vertical surfaces, Int. J. Heat Mass Transf. 40 (1997) 2327–2339.
[8] S.M. Ghiaasiaan, Two-phase Flow, Boiling and Condensation in Conventional and Miniature Systems, Cambridge University Press, New York, 2008.
[9] D.E. Maddox, I. Mudawar, Single- and two-phase convective heat transfer from smooth and enhanced microelectronic heat sources in a rectangular channel, in: H.R. Jacobs (Ed.), Proc. 1988 National Heat Transfer Conf., HTD-Vol. 96, Houston, Texas, 1988, pp. 533–542.
[10] T.C. Willingham, I. Mudawar, Forced-convection boiling and critical heat flux from a linear array of discrete heat sources, Int. J. Heat Mass Transf. 35 (1992) 2879–2890.
[11] C.O. Gersey, I. Mudawar, Effects of heater length and orientation on the trigger mechanism for near-saturated flow boiling CHF – I. Photographic and statistical characterization of the near-wall interfacial features, Int. J. Heat Mass Transf. 38 (1995) 629–642.
[12] J.C. Sturgis, I. Mudawar, Critical heat flux in a long, rectangular channel subjected to one-sided heating - II. Analysis of CHF data, Int. J. Heat Mass Transf. 42 (1999) 1849–1862.
[13] J.A. Shmerler, I. Mudawar, Local heat transfer coefficient in wavy free-falling turbulent liquid films undergoing uniform sensible heating, Int. J. Heat Mass Transf. 31 (1988) 67–77.
[14] I. Mudawar, Recent advances in high-flux, two-phase thermal management, J. Therm. Sci. Eng. Appl. 5 (2013) 021012.
[15] M.K. Sung, I. Mudawar, Experimental and numerical investigation of single-phase heat transfer using a hybrid jet impingement/micro-channel cooling scheme, Int. J. Heat Mass Transf. 49 (2006) 682–694.
[16] M. Monde, T. Inoue, Critical heat flux in saturated forced convective boiling on a heated disk with multiple impinging jets, J. Heat Transf. 113 (1991) 722–727.
[17] D.C. Wadsworth, I. Mudawar, Enhancement of single-phase heat transfer and critical heat flux from an ultra-high-flux simulated microelectronic heat source to a rectangular impinging jet of dielectric liquid, J. Heat Transf. 114 (1992) 764–768.
[18] D.D. Hall, I. Mudawar, Experimental and numerical study of quenching complex-shaped metallic alloys with multiple, overlapping sprays, Int. J. Heat Mass Transf. 38 (1995) 1201–1216.
[19] L. Lin, R. Ponnappan, Heat transfer characteristics of spray cooling in a closed loop, Int. J. Heat Mass Transf. 46 (2003) 3737–3746.
[20] J.D. Bernardin, I. Mudawar, A Leidenfrost point model for impinging droplets and sprays, J. Heat Transf. 126 (2004) 272–278.
[21] I. Mudawar, D. Bharathan, K. Kelly, S. Narumanchi, Two-phase spray cooling of hybrid vehicle electronics, IEEE Trans. – CPMT 32 (2009) 501–512.
[22] M. Visaria, I. Mudawar, Effects of high subcooling on two-phase spray cooling and critical heat flux, Int. J. Heat Mass Transf. 51 (2008) 5269–5278.
[23] I. Mudawar, Two-phase micro-channel heat sinks: theory, applications and limitations, J. Electron. Pack. 133 (2001) 041002-2.
[24] J. Lee, I. Mudawar, Critical heat flux for subcooled flow boiling in micro-channel heat sinks, Int. J. Heat Mass Transf. 52 (2009) 3341–3352.
[25] J. Lee, I. Mudawar, Fluid flow and heat transfer characteristics of low temperature two-phase micro-channel heat sinks – Part 1: Experimental methods and flow visualization results, Int. J. Heat Mass Transf. 51 (2008) 4315–4326.
[26] J.Y. Min, S.P. Jang, S.J. Kim, Effect of tip clearance on the cooling performance of a microchannel heat sink, Int. J. Heat Mass Transf. 47 (2004) 1099–1103.

[27] J.M. Koo, S. Im, L. Jiang, K.E. Goodson, Integrated microchannel cooling for three-dimensional electronic circuit architectures, J. Heat Transf. 127 (2005) 49–58.
[28] I. Mudawar, M.B. Bowers, Ultra-high critical heat flux (CHF) for subcooled water flow boiling – I. CHF data and parametric effects for small diameter tubes, Int. J. Heat Mass Transf. 42 (1999) 1405–1428.
[29] D.D. Hall, I. Mudawar, Ultra-high critical heat flux (CHF) for subcooled water flow boiling – II. High-CHF database and design parameters, Int. J. Heat Mass Transf. 42 (1999) 1429–1456.
[30] S. Mukherjee, I. Mudawar, Smart pumpless loop for micro-channel electronic cooling using flat and enhanced surfaces, IEEE Trans. – CPMT 26 (2003) 99–109.
[31] H. Zhang, I. Mudawar, M.M. Hasan, CHF model for subcooled flow boiling in Earth gravity and microgravity, Int. J. Heat Mass Transf. 50 (2007) 4039–4051.
[32] H. Zhang, I. Mudawar, M.M. Hasan, Experimental assessment of the effects of body force, surface tension force, and inertia on flow boiling CHF, Int. J. Heat Mass Transf. 45 (2002) 4079–4095.
[33] H. Zhang, I. Mudawar, M.M. Hasan, Flow boiling CHF in microgravity, Int. J. Heat Mass Transf. 48 (2005) 3107–3118.
[34] S.H. Lee, I. Mudawar, M.M. Hasan, Thermal analysis of hybrid single-phase, two-phase and heat pump thermal control system (TCS) for future spacecraft, Appl. Therm. Eng. 100 (2016) 190–214.
[35] S. Lee, I. Mudawar, Investigation of flow boiling in large micro-channel heat exchangers in a refrigeration loop for space applications, Int. J. Heat Mass Transf. 97 (2016) 110–129.
[36] S. Lee, I. Mudawar, Transient characteristics of flow boiling in large micro-channel heat exchangers, Int. J. Heat Mass Transf. 103 (2016) 186–202.
[37] S. Lee, I. Mudawar, Thermal and thermodynamic performance, and pressure oscillations of refrigeration loop employing large micro-channel evaporators, Int. J. Heat Mass Transf. 103 (2016) 1313–1326.
[38] J.G. Collier, J.R. Thome, Convective Boiling and Condensation, third ed., Oxford University Press, 1994.
[39] G.E. Geiger, Sudden Contraction Losses in Single and Two-phase Flow Ph.D. Thesis, University of Pittsburgh, Pittsburgh, PA., 1964.
[40] R.K. Shah, A.L. London, Laminar Flow Forced Convection in Ducts: A Source Book for Compact Heat Exchanger Analytical Data (Supl. 1), Academic Press, New York, 1978.
[41] S.W. Churchill, R. Usagi, A general expression for the correlation of rates of transfer and other phenomena, AIChE J. 18 (1972) 1121–1128.
[42] D. Copeland, Manifold microchannel heat sinks: analysis and optimization, ASME/JSME Therm. Eng. 4 (1995) 169–174.
[43] W. Zhi-qing, Study on correction coefficients of laminar and turbulent entrance region effect in round pipe, Appl. Math. Mech. 3 (1982) 433–446.
[44] M.B. Bowers, I. Mudawar, Two-phase electronic cooling using mini-channel and micro-channel heat sinks – Part 2. Flow rate and pressure drop constraints, J. Electron. Pack. 116 (1994) 298–305.
[45] T.L. Bergman, F.P. Incropera, A.S. Lavine, D.P. DeWitt, Fundamentals of Heat and Mass Transfer, seventh ed., Wiley and Sons, New York, 2011.
[46] W.H. McAdams, W.K. Woods, L.C. Heroman, Vaporization inside horizontal tubes. II: Benzene-oil mixtures, Trans. ASME 64 (1942) 193–200.
[47] W.W. Akers, H.A. Deans, O.K. Crosser, Condensing heat transfer within horizontal tubes, Chem. Eng. Prog. 54 (1958) 89–90.
[48] A. Cicchitti, C. Lombardi, M. Silvestri, G. Soldaini, R. Zavattarelli, Two-phase cooling experiments-pressure drop, heat transfer and burnout measurements, Energ. Nucl. 7 (1960) 407–425.
[49] A.E. Dukler, M. Wicks, R.G. Cleveland, Frictional pressure drop in two-phase flow: A. A comparison of existing correlations for pressure loss and holdup, AIChE J. 10 (1964) 38–43.
[50] A.E. Dukler, M. Wicks, R.G. Cleveland, Frictional pressure drop in two-phase flow: B. An approach through similarity analysis, AIChE J. 10 (1964) 44–51.
[51] D.R.H. Beattie, P.B. Whalley, A simple two-phase frictional pressure drop calculation method, Int. J. Multiphase Flow 8 (1982) 83–87.
[52] S. Lin, C.C.K. Kwok, R.-Y. Li, Z.-H. Chen, Z.-Y. Chen, Local frictional pressure drop during vaporization of R-12 through capillary tubes, Int. J. Multiphase Flow 17 (1991) 95–102.
[53] R.W. Lockhart, R.C. Martinelli, Proposed correlation of data for isothermal two-phase, two-component flow in pipes, Chem. Eng. Prog. 45 (1949) 39–48.
[54] S.M. Zivi, Estimation of steady-state steam void-fraction by means of the principle of minimum entropy production, J. Heat Transf. 86 (1964) 247–252.
[55] S.Z. Rouhani, E. Axelsson, Calculation of void volume fraction in the subcooled and quality boiling regions, Int. J. Heat Mass Transf. 13 (1970) 383–393.
[56] M.A. Woldesemayat, A.J. Ghajar, Comparison of void fraction correlations for different flow patterns in horizontal and upward inclined pipes, Int. J. Multiphase Flow 33 (2007) 347–370.
[57] S.-M. Kim, I. Mudawar, Universal approach to predicting two-phase frictional pressure drop for mini/micro-channel saturated flow boiling, Int. J. Heat Mass Transf. 58 (2013) 718–734.
[58] D. Chisholm, Pressure gradients due to friction during the flow of evaporating two-phase mixtures in smooth tubes and channels, Int. J. Heat Mass Transf. 16 (1973) 347–358.
[59] L. Friedel, Improved friction pressure drop correlations for horizontal and vertical two-phase pipe flow, in: European Two-Phase Flow Group Meeting, Ispra, Italy, Paper E2, 1979.
[60] H. Müller-Steinhagen, K. Heck, A simple friction pressure drop correlation for two-phase flow in pipes, Chem. Eng. Process. 20 (1986) 297–308.
[61] K. Mishima, T. Hibiki, Some characteristics of air-water two-phase flow in small diameter vertical tubes, Int. J. Multiphase Flow 22 (1996) 703–712.
[62] T.N. Tran, M.-C. Chyu, M.W. Wambsganss, D.M. France, Two-phase pressure drop of refrigerants during flow boiling in small channels: an experimental investigation and correlation development, Int. J. Multiphase Flow 26 (2000) 1739–1754.
[63] H.J. Lee, S.Y.Y. Lee, Pressure drop correlations for two-phase flow within horizontal rectangular channels with small heights, Int. J. Multiphase Flow 27 (2001) 783–796.
[64] W. Qu, I. Mudawar, Measurement and prediction of pressure drop in two-phase micro-channel heat sinks, Int. J. Heat Mass Transf. 46 (2003) 2737–2753.
[65] L. Sun, K. Mishima, Evaluation analysis of prediction methods for two-phase flow pressure drop in mini-channels, Int. J. Multiphase Flow 35 (2009) 47–54.
[66] W. Zhang, T. Hibiki, K. Mishima, Correlations of two-phase frictional pressure drop and void fraction in mini-channel, Int. J. Heat Mass Transf. 53 (2010) 453–465.
[67] R. Revellin, V. Dupont, T. Ursenbacher, J.R. Thome, I. Zun, Characterization of diabatic two-phase flows in microchannels: flow parameter results for R-134a in a 0.5 mm channel, Int. J. Multiphase Flow 32 (2006) 755–774.
[68] G. Wang, P. Cheng, A.E. Bergles, Effects of inlet/outlet configurations on flow boiling instability in parallel microchannels, Int. J. Heat Mass Transf. 51 (2008) 2267–2281.
[69] R. Revellin, J.R. Thome, A new type of diabatic flow pattern map for boiling heat transfer in microchannels, J. Micromech. Microeng. 17 (2007) 788–796.
[70] S. Saitoh, H. Daiguji, E. Hihara, Effect of tube diameter on boiling heat transfer of R-134a in horizontal small-diameter tubes, Int. J. Heat Mass Transf. 48 (2005) 4973–4984.